Distributed situational observer in a displaced orbit: relative dynamics and control

Xiao Pan
Ming Xu

Distributed situational observer in a displaced orbit: relative dynamics and control

Xiao Pan and Ming Xu*
Beihang University, School of Astronautics, Beijing, China

Abstract. We design a distributed situational observer using formation flying in a displaced orbit. The main focus of our investigation is the relative dynamics and control of displaced orbits obtained by low-thrust propulsion. The spatial dynamics in Newtonian form are used to derive the numerical relative motions, and their natural frequencies discovered by eigenvalue decomposition separate from each other at a critical height that differentiates the structural stability, bifurcation, and instability. Using the Jordan decomposition, six fundamental motions are achieved, including the stationary multiequilibria, the periodic oscillations that correspond to the natural frequencies, and the maximum leaving or approaching velocity caused by the different geometric and algebraic multiplicities. Off-axis equilibrium is obtained by a proposed open-loop control, and the motions nearby are proven to be equivalent to the numerical relative motions. The reduced dynamics in Hamiltonian form are used to derive the analytical solutions for linearized relative motions. Bounded relative trajectories with arbitrary initial values are achieved by two extraclosed-loop controls. Using the off-axis equilibrium and resonance of natural frequencies, the applications of a fixed relative baseline vector for interferometric SAR or Fresnel zone lens missions and repeating relative ground tracks for a phased array antenna mission are addressed in terms of the trajectory design. © *The Authors. Published by SPIE under a Creative Commons Attribution 3.0 Unported License. Distribution or reproduction of this work in whole or in part requires full attribution of the original publication, including its DOI.* [DOI: 10.1117/1.JATIS.4.4.045001]

Keywords: linearized relative motions; displaced circular orbit; low thrust; reduced dynamics; formation flying.

Paper 18038 received Jun. 11, 2018; accepted for publication Oct. 15, 2018; published online Nov. 8, 2018.

1 Introduction

Large families of displaced orbits have been identified by solar sail or electric propulsion thrusters in the context of the non-Keplerian two-body problem including three types of circular orbits by propulsive acceleration,[1–3] quasiperiodic displaced trajectories by a fixed thrust along the rotation axis of a planet,[4] body-fixed hovering orbits by open-loop control,[5] elliptic displaced orbits with an advanced thrust model,[6] a sequence of individual Keplerian arcs connected by slight impulse propulsion,[7] and a displaced geostationary orbit (GEO) using hybrid sail propulsion.[8] A large catalog of these orbits was provided by McKay et al.[9] for motions around planetary bodies. The use of continuous low-thrust propulsion to generate artificial equilibria or displaced orbits above a planet has potential applications in astronomical missions, such as observing Saturn's rings *in situ*, monitoring solar wind, and hovering above dangerous asteroids. An interesting mission scenario involving displaced orbits is offered by a concept for an Earth–Mars interplanetary communications relay,[10] which supports a future manned mission toward Mars and accomplishes both real-time observation and telecommunication tasks.

Some sensing measurement applications for displaced orbits require very long or distributed baselines, which are beyond the capability of a single spacecraft. Fractionated architectures offer a possible solution to this problem by employing multiple satellites that operate in proximity of each other (i.e., formation flying). The topic of formation flying on a Keplerian orbit has been widely investigated in previous years, and plentiful results were summarized by Alfriend et al.[11] However, less

attention was paid to the formation flying of a displaced orbit. Biggs and McInnes[12] considered formation flying in a solar-sail elliptical restricted three-body problem and identified a family of 1-year periodic orbits in which each orbit corresponds to a unique solar sail orientation using a numerical continuation method. However, they did not address the relative dynamics of displaced orbits. Gong et al.[13] investigated the solar-sail-propelled formation flying around heliocentric displaced orbits as well as the formation around planetary displaced orbits for geocentric and Martian cases.[14] The relative motion was formulized by the simple variational equation of two-body dynamics and the focus of investigation is on the analysis of the stable region and control laws. Although the same as this paper is that the relative dynamics is linearized, neither Ref. 13 nor Ref. 14 gave a linear analytical solution and dealt with the practical applications of solar-sail formations. McInnes[7] linearized the relative motion in a rotating frame of reference and obtained analytical solutions, but no propulsive acceleration was included. Wang et al.[15] worked on the relative motions between the two heliocentric circular displaced orbits by defining a set of displaced orbital elements and obtained a semianalytical approximation of bounds of relative distance. Later, they generalized the theory and methodology to the elliptic orbits in Ref. 16, and further extended the analysis to avoid failure by eliminating the singularities of classical orbital elements.[17] However, the methodologies of Wang[15–17] apply only to the formation around periodic displaced orbits, not to quasiperiodic orbits. In addition, Wang et al. succeeded in predicting the inner and outer bounds of relative motion, but they did not consider the spacecraft proximity operations and control strategies, which are illuminated in this paper.

To design the distributed situational observer, the formation flying and operation in proximity of a displaced orbit are

---

*Address all correspondence to: Ming Xu, E-mail: xuming@buaa.edu.cn

investigated in this paper, and the linearized relative motions around a displaced circular orbit are derived. First, the spatial dynamics in Newtonian form are used to derive the numerical relative motions. The natural frequencies are solved by eigenvalue decomposition, and the six fundamental motions are classified by the Jordan decomposition, including the stationary multiequilibria, the periodic oscillations that correspond to the natural frequencies, and the maximum leaving or approaching velocity. Second, an extra open-loop control is proposed to achieve off-axis equilibrium, and the nearby motions are proved to be equivalent to the numerical relative motions. Third, the reduced dynamics in Hamiltonian form are utilized to derive the analytical solutions for relative motions, and two extra-closed-loop controls are developed to yield bounded relative trajectories regardless of the initial values for all displaced height cases. Finally, the applications of relative motions around displaced orbits are addressed for the fixed relative baseline vector for interferometric synthetic aperture radar (InSAR) or Fresnel zone lens missions and repeating relative ground tracks for a phased array antenna mission.

2 Dynamics of a Displaced Circular Orbit Maintained by a Low-Thrust Propulsion System

A displaced orbit relies on the low-thrust propulsion system to hover above the Earth at a certain height during the lifetime of a spacecraft. The dynamics of the chief spacecraft (denoted by chief in the following sections) with the propulsive acceleration can be written both in the Earth-centered inertial frame $I(x_i, y_i, z_i)$ and cylindrical coordinate frame $C(\rho, h, \phi)$. In the former frame, the displaced dynamics is treated as a three degree-of-freedom (DOF) system, but in the latter frame, it is two and one-half DOF. Therefore, to differentiate, the dynamics modeled in the (x, y, z) space is referred to as the spatial dynamics, whereas in the (ρ, h, ϕ) space referred to as the reduced dynamics.

2.1 Spatial Dynamics of a Displaced Circular Orbit Maintained by Low-Thrust Propulsion System

The standard dynamics of the chief spacecraft (denoted by chief in the following sections) with the propulsive acceleration can be written in the Earth-centered inertial frame $I(x_i, y_i, z_i)$ as

$$\ddot{\mathbf{r}}_i = -\nabla_i U + \mathbf{a}_i, \tag{1}$$

where $\mathbf{r}_i$ is the position vector from the spacecraft to the inertial frame origin, i.e., the center of the Earth, $\mathbf{a}_i$ is the propulsive acceleration in the Earth-centered inertial frame, and U is the gravitational potential $U = -\mu/\|\mathbf{r}_i\|$, where μ is the gravitational parameter of the Earth and the gradient operator in the frame is $\nabla_i = \begin{bmatrix} \frac{\partial}{\partial x_i} & \frac{\partial}{\partial y_i} & \frac{\partial}{\partial z_i} \end{bmatrix}^T$.

Another frame, which is named the first orbital frame $\mathbf{O}(x_o, y_o, z_o)$, is defined as follows and shown in Fig. 1: the origin is the spacecraft, the x_o axis points along the direction from the Earth to spacecraft, the z_o axis is located inside the plane formed by the x_o- and the zi-axes perpendicular to the x_o axis, and the y_o axis can be determined by the right-hand rule. The angle between the x_o axis and z_i axis is defined as θ, and the angle between the x_i axis and the (x_o, z_o) plane is defined as ϕ. For the circular displaced orbit case, the y_o axis points along the velocity direction of the chief, θ remains invariant, and ϕ is linear with the time according to $\phi = \omega t$, where ω is the angular velocity of the displaced circular orbit and t is the flying time.

To maintain a displaced circular orbit, there must be a constant propulsive acceleration with a fixed direction in the (ρ, h) plane or (x_o, z_o) plane whose magnitude a and direction angle α with respect to the z_i axis are achieved as[3]

$$a(\rho, h; \omega) = \sqrt{\rho^2(\omega^2 - \omega_*^2)^2 + h^2\omega_*^4}, \tag{2}$$

$$\tan \alpha(\rho, h; \omega) = \frac{\rho}{h}\left[1 - \left(\frac{\omega}{\omega_*}\right)^2\right], \tag{3}$$
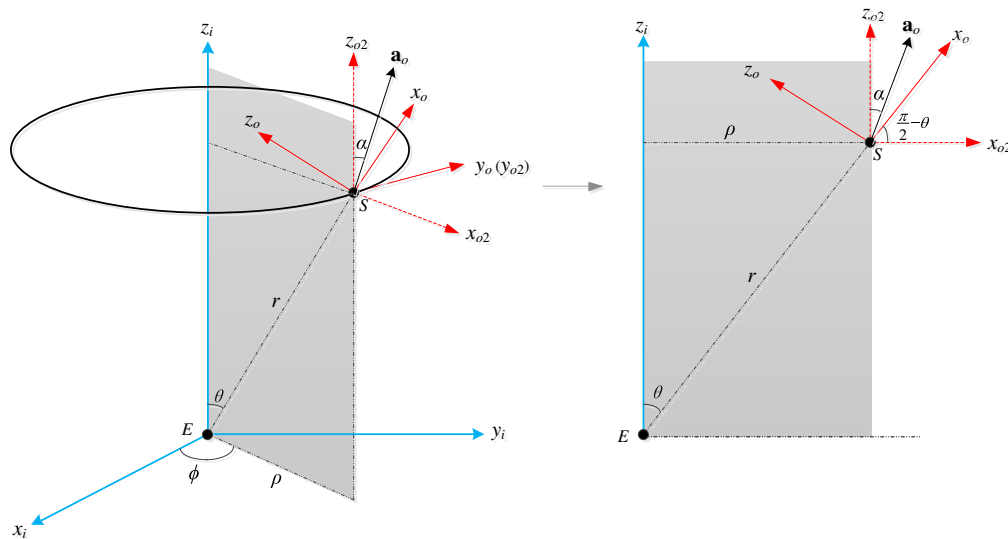

Fig. 1 Geometry of displaced circular orbit: E denotes the Earth, and S denotes spacecraft; E-$x_i y_i z_i$ is the Earth-centered inertial frame I, S-$x_o y_o z_o$ is the spacecraft-centered orbital frame $\mathbf{O}$, and S-$x_{o2} y_{o2} z_{o2}$ is the spacecraft-centered second orbital frame $\mathbf{O}_2$.

where ω_* is the orbital angular velocity of a circular Keplerian orbit with a radius equal to the radius of the displaced orbit, i.e., $\omega_* = \sqrt{\mu/r^3} = \sqrt{\mu/(\rho^2 + h^2)^{\frac{3}{2}}}$. Thus, the propulsive acceleration $\mathbf{a}_o$ in the $\mathbf{O}$ frame is derived as

$$\mathbf{a}_o = a[\cos(\theta - \alpha) \quad 0 \quad \sin(\theta - \alpha)]^T. \tag{4}$$

As ω is constant, the y_o component of $\mathbf{a}_o$ must be zero, and the $\mathbf{a}_o$ direction can be described by the pitch angle $(\theta - \alpha)$.

2.2 Reduced Dynamics of a Displaced Circular Orbit Maintained by Low-Thrust Propulsion System

Using the Hamiltonian method, the reduced dynamics of the chief in the (ρ, h, ϕ) space can be derived as[18]

$$\begin{cases} \ddot{\rho} = \frac{h_z^2}{\rho^3} - \mu \frac{\rho}{r^3} + a \sin \alpha \\ \ddot{h} = -\mu \frac{h}{r^3} + a \cos \alpha \end{cases}, \tag{5}$$

$$\ddot{\phi} = -\frac{2\dot{\rho}\dot{\phi}}{\rho}, \tag{6}$$

where $h_z = \rho^2 \dot{\phi}$ is the constant angular momentum directed along the z_i or z_o axis, which can be yielded from Eq. (6), ρ is the orbital radius projected on the (x_i, y_i) plane and h is the coordinate component on the z_i axis, r is the distance between the chief spacecraft and the Earth, $r = \sqrt{\rho^2 + h^2}$.

The potential energy can be written as

$$U = -\mu/r - a \cos \alpha \cdot h - a \sin \alpha \cdot \rho. \tag{7}$$

The propulsive acceleration in the (ρ, h) space, i.e., $a = a[\sin \alpha, \cos \alpha]^T$ in Eq. (5), is independent of time but dependent on the position components ρ and h. Thus, a closed-loop control strategy[19] of low thrust with the feedback of ρ and h can be considered, and all the trajectories discussed in this paper are generated by the same strategy, which is referred to as basic propulsive acceleration (BPA) in the following sections.

This system has two equilibria: the first equilibrium is the elliptic (stable) topological type, and the second equilibrium is hyperbolic (unstable).[4] The stable equilibrium point is mapped onto the displaced circular orbit adopted by the chief, and the bounded trajectories are mapped onto the quasiperiodic displaced orbits adopted by the follower.

The reduced dynamics present a simple understanding of the motions in the (ρ, h) space; however, the ϕ component remains ambiguous. Even though the natural boundedness on the ρ and h components can help the follower maintain bounded relative motions to the chief, the unsuited ϕ component will drive it away from the chief. To solve this problem, the linearized motion derived from the spatial dynamics is analyzed in the next section to design the bounded relative trajectories.

3 Linearized Relative Motions in a Displaced Circular Orbit Derived from Spatial Dynamics

3.1 Linearized Relative Motions Derived from Spatial Dynamics

The coordinate transformation matrix from the $\mathbf{O}$ frame to the $\mathbf{I}$ frame is given as

$$\mathbf{F}(\theta, \phi) = \mathbf{R}_z(-\phi)\mathbf{R}_y\left(\frac{\pi}{2} - \theta\right), \tag{8}$$

where $\mathbf{R}_y$ and $\mathbf{R}_z$ are the fundamental transformation matrixes along the y and z-axes. The gradient operator in the $\mathbf{O}$ frame is $\nabla = [\frac{\partial}{\partial r} \quad \frac{1}{r}\frac{\partial}{\partial\theta} \quad \frac{1}{r\sin\theta}\frac{\partial}{\partial\varphi}]^T$. The relative position vector of the follower to the chief in the $\mathbf{I}$ frame is denoted by $\Delta\mathbf{r}_i$, and that in the $\mathbf{O}$ frame is denoted by $\Delta\mathbf{r}_o = [x_o, y_o, z_o]^T$; then, the relationship between them is differentiated as $\Delta\mathbf{r}_i = \mathbf{F} \cdot \Delta\mathbf{r}_o$, which yields

$$\Delta\ddot{\mathbf{r}}_i = \mathbf{F} \cdot \Delta\ddot{\mathbf{r}}_o + 2\dot{\mathbf{F}} \cdot \Delta\dot{\mathbf{r}}_o + \ddot{\mathbf{F}} \cdot \Delta\mathbf{r}_o. \tag{9}$$

The gravitational potential function of the follower is

$$U^F = -\frac{\mu}{\sqrt{(r + x_o)^2 + y_o^2 + z_o^2}}, \tag{10}$$

U^F will degenerate into the chief's potential function when $\Delta\mathbf{r}_o = [0,0,0]^T$, i.e., $U^C = U^F|_{(x,y,z)=(0,0,0)}$.

Compared with the only BPA denoted $\mathbf{a}^C$ of the chief, the propulsive acceleration imposed on the follower includes the BPA denoted $\mathbf{a}^F$ and the extra BPA denoted $\mathbf{u}_i$ in the $\mathbf{I}$ frame and $\mathbf{u}_o$ in the $\mathbf{O}$ frame. In the inertial frame, the relative dynamics can be written as $\Delta\ddot{\mathbf{r}}_i = -\nabla U^F + \nabla U^C + \Delta\mathbf{a}_i + \mathbf{u}_i$, where $\Delta\mathbf{a}_i$ is the difference between the BPA of the chief $\mathbf{a}^C$ and the BPA of the follower $\mathbf{a}^F$, which can be simplified by the Taylor linearization as

$$\begin{aligned}\Delta\ddot{\mathbf{r}}_i &= -\nabla(U^F - U^C) + \Delta\mathbf{a}_i + \mathbf{u}_i \\ &= -\nabla(\nabla_{\Delta\mathbf{r}_o} U^F|_{\Delta\mathbf{r}_o=0} \cdot \Delta\mathbf{r}_o) + \Delta\mathbf{a}_i + \mathbf{u}_i \\ &= -\mathbf{F} \cdot (\nabla \cdot \nabla_{\Delta\mathbf{r}_o})U^F|_{\Delta\mathbf{r}_o=0} \cdot \Delta\mathbf{r}_o + \Delta\mathbf{a}_i + \mathbf{u}_i, \end{aligned} \tag{11}$$

where the linear operator $\nabla_{\Delta\mathbf{r}}$ is defined as $\nabla_{\Delta\mathbf{r}_o} = [\frac{\partial}{\partial x} \quad \frac{\partial}{\partial y} \quad \frac{\partial}{\partial z}]^T$. Combined with Eq. (9), the linear operators ∇ and $\nabla_{\Delta\mathbf{r}}$ can exchange their operating turns to yield

$$\begin{aligned}\Delta\ddot{\mathbf{r}}_o + 2\mathbf{F}^{-1}\dot{\mathbf{F}}\Delta\dot{\mathbf{r}}_o + \mathbf{F}^{-1}\ddot{\mathbf{F}}\Delta\mathbf{r}_o + (\nabla_{\Delta\mathbf{r}_o} \cdot \nabla)U^F|_{\Delta\mathbf{r}_o=0} \cdot \Delta\mathbf{r}_o \\ = \Delta\mathbf{a}_o + \mathbf{u}_o. \end{aligned} \tag{12}$$

Here, $\mathbf{a}^C$ and $\mathbf{a}^F$ have the same form of $[\cos(\theta - \alpha), 0, \sin(\theta - \alpha)]^T$ in the chief's orbital frames and follower's orbital frames, respectively, and the relative BPA is written as

$$\begin{aligned}\Delta\mathbf{a}_o &= [\mathbf{F}^{-1}(\theta, \phi^F) \cdot \mathbf{F}(\theta, \phi^C) - \mathbf{I}] \\ &\quad \cdot [a\cos(\theta - \alpha) \quad 0 \quad a\sin(\theta - \alpha)]^T \\ &= [0 \quad -a \cdot \sin\alpha \cdot \Delta\phi \quad 0]^T, \end{aligned} \tag{13}$$

where $\Delta\phi = \phi^F - \phi^C$ is derived from the relative position between the chief and follower, $\Delta\mathbf{r}_o = [x_o, y_o, z_o]^T$.
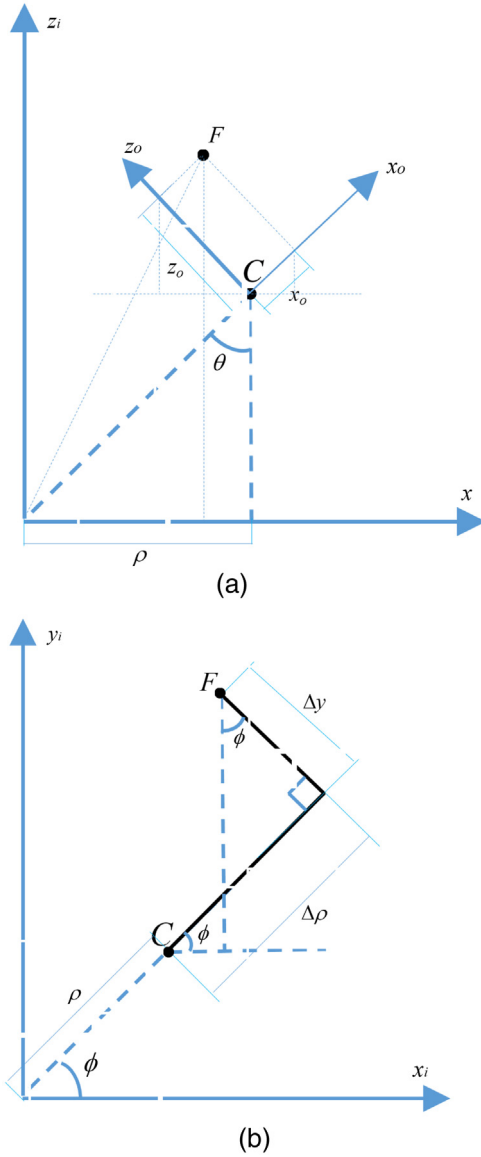
Fig. 2 Relative geometry between the chief and follower: (a) the relationship among $\Delta\rho$, x_o, and z_o in the x-z_i plane (the x axis is defined in the following $\mathbf{O}_2$ frame); (b) the relationship between $\Delta\phi$ and y_o in the x_i-y_i plane.

According to the definition of ϕ in Eqs. (5) and (6), i.e., $\tan\phi^C = \rho\sin\phi^C/\rho\cos\phi^C$, and the relative geometry shown in Fig. 2

$$\tan\phi^F = \frac{\rho\sin\phi^C + (x_o\sin\theta - z_o\cos\theta)\sin\phi^F + y_o\cos\phi^F}{\rho\cos\phi^C + (x_o\sin\theta - z_o\cos\theta)\cos\phi^F - y_o\sin\phi^F},$$

$$(14)$$

$$\Delta\rho = x_0\sin\theta - z_0\cos\theta, \qquad y_o = \rho\cdot\Delta\phi. \quad (15)$$

Combining Eqs. (8), (12), (13), and (15) yields the linearized relative motion as

$$\Delta\ddot{\mathbf{r}}_o + \mathbf{A}\Delta\dot{\mathbf{r}}_o + \mathbf{B}\Delta\mathbf{r}_o = \mathbf{u}_o, \quad (16)$$

where

$$\mathbf{A} = -2\omega\begin{bmatrix} 0 & \sin\theta & 0 \\ -\sin\theta & 0 & \cos\theta \\ 0 & -\cos\theta & 0 \end{bmatrix},$$

$$\mathbf{B} = \omega^2\begin{bmatrix} -\sin^2\theta & 0 & \sin\theta\cos\theta \\ 0 & -1 & 0 \\ \sin\theta\cos\theta & 0 & -\cos^2\theta \end{bmatrix}$$

$$+ \omega_*^2\begin{bmatrix} -2 & 0 & 0 \\ 0 & 1 & 0 \\ 0 & 0 & 1 \end{bmatrix} + \frac{\sin\alpha\cdot a}{\rho}\begin{bmatrix} 0 & 0 & 0 \\ 0 & -1 & 0 \\ 0 & 0 & 0 \end{bmatrix}. \quad (17)$$

For a Keplerian circular orbit, when the displaced height h degenerates into zero, θ becomes $\pi/2$, and Eq. (16) degenerates into the classic Clohessy–Wiltshire (C-W) equation.

The second orbital frame $\mathbf{O}_2(x_{o2}, y_{o2}, z_{o2})$ is introduced with the x_{o2} axis pointing along the ρ direction, the z_{o2} axis pointing along the z_i direction, and the y_{o2} axis following the right-hand rule. The frame $\mathbf{O}_2$ is formed through rotating frame $\mathbf{O}$ by $\pi/2 - \theta$ counterclockwise around the y_o axis, thus, the relative position vector $\Delta\mathbf{r} = [x, y, z]^T$ in the $\mathbf{O}_2$ frame can be achieved from $\Delta\mathbf{r} = \mathbf{R}_y(\pi/2 - \theta)\cdot\Delta\mathbf{r}_o$. Then, the linearized relative motion can be transformed as

$$\Delta\ddot{\mathbf{r}} + \tilde{\mathbf{A}}\Delta\dot{\mathbf{r}} + \tilde{\mathbf{B}}\Delta\mathbf{r} = \mathbf{u}, \quad (18)$$

where

$$\tilde{\mathbf{A}} = \omega\begin{bmatrix} 0 & -2 & 0 \\ 2 & 0 & 0 \\ 0 & 0 & 0 \end{bmatrix},$$

$$\tilde{\mathbf{B}} = \omega^2\begin{bmatrix} -1 & 0 & 0 \\ 0 & -1 & 0 \\ 0 & 0 & 0 \end{bmatrix}$$

$$+ \omega_*^2\begin{bmatrix} 1 - 3\sin^2\theta & 0 & -3\sin\theta\cos\theta \\ 0 & 1 & 0 \\ -3\sin\theta\cos\theta & 0 & 1 - 3\cos^2\theta \end{bmatrix}$$

$$+ \frac{\sin\alpha\cdot a}{\rho}\begin{bmatrix} 0 & 0 & 0 \\ 0 & -1 & 0 \\ 0 & 0 & 0 \end{bmatrix}. \quad (19)$$

Analytical solutions are difficult to obtain for both Eqs. (16) and (18) due to the nonzero θ. The following numerical implementations are used to verify the linearized relative motions compared with the nonlinear chief's dynamics subtracted from the follower's dynamics.

For a scenario consisting of a displaced orbit above the GEO at a height $h = 150$ km having the radius of circular orbit $\rho = r_{\text{GEO}} = 42,164.1696$ km and the angular velocity of $\omega = \omega_{\text{GEO}}$, both the linearized relative motions and nonlinear relative motions are propagated from the initial condition as $\Delta x = \Delta y = \Delta z = 100$ m, $\Delta\dot{x} = \Delta\dot{y} = 0$, and $\Delta\dot{z} = 1$ m/s in the $\mathbf{O}_2$ frame, as shown in Fig. 3. The linearized equation derived in this section coincides with the nonlinear equation, and the maximum relative error (MRE) in the along-track direction is 2.25% during 10 orbital periods. The accuracy of
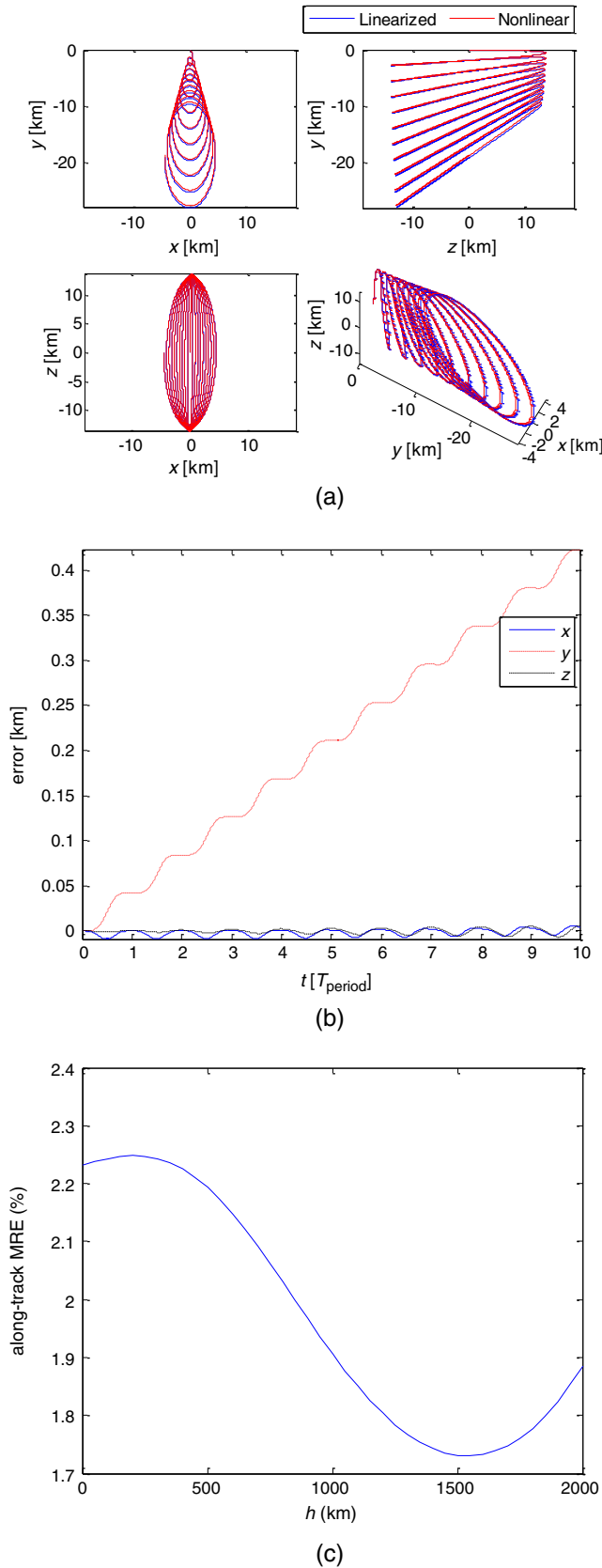
(a)

(b)

(c)

Fig. 3 Comparison between the linearized and nonlinear relative motions: (a) relative trajectory: views and 3-D plot in the $\mathbf{O}_2$ frame; (b) the time history of the errors between them; (c) MRE in the along-track direction for different displaced heights.

the linearized equation is evaluated by comparison with the MRE of C-W equations for formation around Keplerian orbits. When the displaced height is 0, the linearized equations derived in this section degenerate to the C-W equations, whose MRE in the along-track direction is 2.22%. Since the accuracy of relative motions described by C-W equations is accepted generally, the linearized equations in this section whose MRE is the same order as errors of C-W equations are accurate enough to model the nonlinear relative motions in the following sections. Furthermore, this accuracy is checked for many different displaced heights in Fig. 3(c). Even if a more accurate result is required, the linearized equations can serve as a very good initial value for a developed iteration algorithm.

3.2 Solutions of Linearized Relative Motions Derived from Spatial Dynamics

In contrast to the classic C-W equation modeled on Keplerian circular orbits, the linearized Eqs. (16) and (18) are difficult to solve analytically. Thus, the natural properties of their solutions will be discussed in this section by matrix decomposition methods.

The eigenvalue decomposition method is used to investigate the natural frequencies in Eq. (16) or Eq. (18). Taking the displaced GEO ($\rho = r_{GEO}$, $\omega = \omega_{GEO}$) e.g., the eigenvalues of linearized equation are characterized by the height h. Here, the value of h is traversed from 0 to 60,000 km with the step size of 100 km to investigate the evolutions of the eigenvalues. It is found that there exists a critical value of h, i.e., $h_{cri} = 18,700$ km, which can classify the different eigenvalue spectrum. When the height is less than $h_{cri} = 18,700$ km, the eigenvalue spectrum consists of a pair of zero eigenvalues and two pairs of conjugate imaginary eigenvalues, i.e., 0, 0, $\pm\omega_2 i$, and $\pm\omega_3 i$. Thus, ω_2 and ω_3 are referred to as the natural frequencies, and their relationship with the height is shown in Fig. 4. For the special case $h = 0$ km, ω_2 is equal to ω_3. When the height is h_{cri}, ω_2 degenerates into zero, so the eigenvalue spectrum consists of two pairs of zero eigenvalues and a pair of conjugate imaginary eigenvalues, i.e., 0, 0, 0, 0, and $\pm\omega_3 i$. When the height exceeds h_{cri}, the eigenvalue spectrum consists of a pair of conjugate imaginary eigenvalues, a pair of real eigenvalues, and a pair of zero eigenvalues, i.e., 0, 0, $\pm\omega i$, and $\pm\lambda$. Since in this simulation there is a one-to-one correspondence between the height h and angle θ, there also exists a critical value of θ, which plays the same role as the h_{cri}. The analysis and results below are carried out based on the different displaced heights h or, in other words, different values of θ. Furthermore, the following results can also generalize to other relative orbits with $\rho \neq r_{GEO}$, $\omega \neq \omega_{GEO}$, in which scenario there still exists a h_{cri} to differentiate the eigenvalues, but its value is changed rather than 18,700 km.

From the linear stability theory point of view, the positive real eigenvalue $+\lambda$ in the $h > h_{cri}$ case indicates the instability of relative motions; however, the zero eigenvalue for the $h < h_{cri}$ case cannot yield the same conclusion. Thus, the Jordan decomposition is used to investigate the linearized relative motions, which is one of the contributions developed in this paper.

For the scenarios in which the follower flies ahead or behind the chief on the same displaced circular orbit, the existence of multiequilibria on the along-track direction in Eq. (16) or
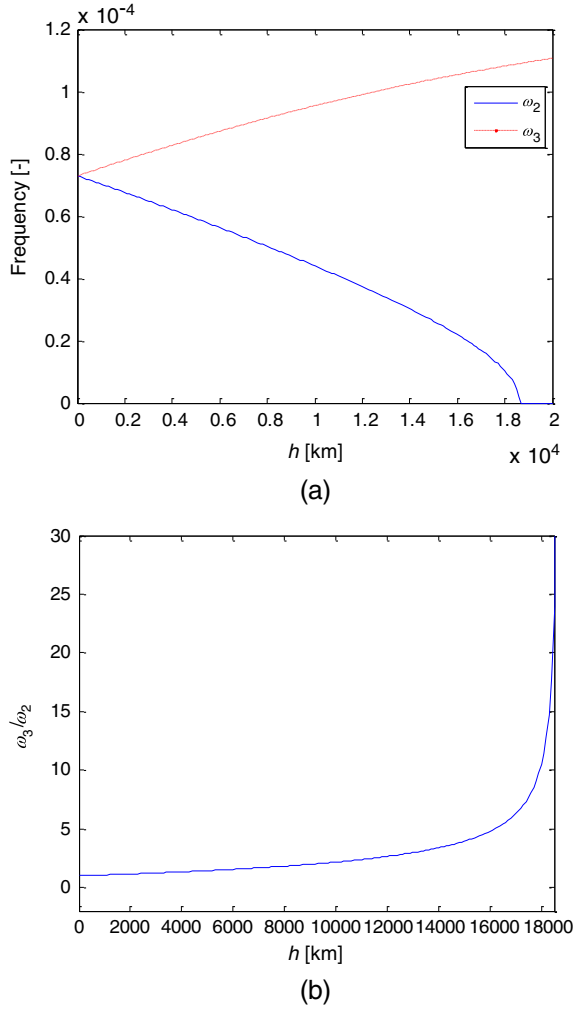
$$\mathbf{\Phi} \cdot [\mathbf{q}_1, \mathbf{q}_2, \mathbf{q}_3, \mathbf{q}_4, \mathbf{q}_5, \mathbf{q}_6] = [\mathbf{q}_1, \mathbf{q}_2, \mathbf{q}_3, \mathbf{q}_4, \mathbf{q}_5, \mathbf{q}_6] \cdot \mathbf{J},$$

$$\mathbf{J} = \begin{bmatrix} 0 & 1 & & & & \\ & 0 & & & & \\ & & 0 & -\omega_2 & & \\ & & \omega_2 & 0 & & \\ & & & & 0 & -\omega_3 \\ & & & & \omega_3 & 0 \end{bmatrix}, \qquad (22)$$

where all blank elements in $\mathbf{J}$ are zeros. Equation (22) can be expanded to yield $\mathbf{\Phi} \cdot \mathbf{q}_1 = \mathbf{0}$, $\mathbf{\Phi} \cdot \mathbf{q}_2 = \mathbf{q}_1, \ldots,$ and these two equations can be combined to gain $\mathbf{\Phi}^2 \cdot \mathbf{q}_2 = \mathbf{\Phi} \cdot \mathbf{q}_1 = \mathbf{0}$. Therefore, Φ^2 has two eigenvectors with a zero eigenvalue, one of which is $\mathbf{q}_1$, which was proven in the previous section. Therefore, $\mathbf{q}_2$ is the other eigenvector with a zero eigenvalue.

For any $\mathbf{z}(t)_{6 \times 1}$, the state $\mathbf{X}$ spanned by $\mathbf{X} = [\mathbf{q}_1, \mathbf{q}_2, \mathbf{q}_3, \mathbf{q}_4, \mathbf{q}_5, \mathbf{q}_6] \cdot \mathbf{z} = \mathbf{Q} \cdot \mathbf{z}$ is substituted into $\dot{\mathbf{X}} = \mathbf{\Phi}\mathbf{X}$ to yield, with the help of Eq. (22), $\mathbf{Q} \cdot \dot{\mathbf{z}} = \mathbf{\Phi}\mathbf{Q} \cdot \mathbf{z} = \mathbf{Q}\mathbf{J} \cdot \mathbf{z}$. For the simplified system $\dot{\mathbf{z}} = \mathbf{J}\mathbf{z}$, the general solution can be written as $\mathbf{z}(t) = e^{\mathbf{J}t}\mathbf{z}(0)$, where $\mathbf{z}(0)$ is any initial vector and the term $e^{\mathbf{J}t}$ is expanded as

$$e^{\mathbf{J}t} = \begin{bmatrix} 1 & t & & & & \\ & 1 & & & & \\ & & c\,\omega_2 t & -s\,\omega_2 t & & \\ & & s\,\omega_2 t & c\,\omega_2 t & & \\ & & & & c\,\omega_3 t & -s\,\omega_3 t \\ & & & & s\,\omega_3 t & c\,\omega_3 t \end{bmatrix}. \qquad (23)$$

The components of $\mathbf{z}(t)$ can be solved as $\mathbf{z}_1(t) = \mathbf{z}_1(0) + \mathbf{z}_2(0) \cdot t$, $\mathbf{z}_2(t) = \mathbf{z}_2(0)$, $\mathbf{z}_3(t) = \mathbf{z}_3(0) \cdot c\omega_2 t - \mathbf{z}_4(0) \cdot s\omega_2 t, \ldots,$ where $\mathbf{z}_i$, $i = 1, 2, \ldots, 6$, is the i'th component of $\mathbf{z}$. The first $\mathbf{z}_1(t) = \mathbf{z}_1(0) + \mathbf{z}_2(0) \cdot t$ indicates that the only "zero" condition that maintains the bounded relative trajectories is $\mathbf{z}_2(0) = 0$.

Based on the previous statements, the general state $\mathbf{X}$ can be solved as

$$\mathbf{X} = [\mathbf{q}_1, \mathbf{q}_2, \mathbf{q}_3, \mathbf{q}_4, \mathbf{q}_5, \mathbf{q}_6]e^{\mathbf{J}t} \times \mathbf{z}(0), \qquad (24)$$

where $\mathbf{q}_i$, $i = 1, 2, \ldots, 6$, serve as the initial values of the six fundamental motions, $[\mathbf{q}_1, \mathbf{q}_2, \mathbf{q}_3, \mathbf{q}_4, \mathbf{q}_5, \mathbf{q}_6]e^{\mathbf{J}t}$ gives the evolution of the fundamental motions at any moment t, and $\mathbf{z}(0)$ is the linear combination coefficient of $\mathbf{q}_i$ used to select the different fundamental motions for specified missions.

The first motion propagated from $\mathbf{q}_1$ will remain stationary in the along-track direction, i.e., $\Delta y = \mathbf{q}_1 \cdot \mathbf{z}_1(t) = \mathbf{z}_1(0)$, as shown in Fig. 5(a). The second motion propagated from $\mathbf{q}_2$ provides the follower with the maximum along-track velocity leaving or approaching the chief with no velocity in other directions, as shown in Fig. 5(b). According to the numerical results, $\mathbf{q}_2$ has the form $\mathbf{q}_2 = [x_0 \ \ 0 \ \ z_0 \ \ 0 \ \ \dot{y}_0 \ \ 0]^T$, and the relationships between the displaced height h and the ratios of $x_0/\dot{y}_0$ and the relationships between h and $z_0/\dot{y}_0$ are shown in Fig. 6. The z_0 component degenerates into zero in the Keplerian case, and the other components $x_0 = -\frac{2}{3}\frac{\dot{y}_0}{\omega}$ satisfy the requirements of eliminating the first term (corresponding to $\mathbf{q}_1$), third term, and fourth term (corresponding to $\mathbf{q}_3/\mathbf{q}_4$ and $\mathbf{q}_5/\mathbf{q}_6$) in the along-track motion of the classic C-W equation, i.e., the y axis as[20]
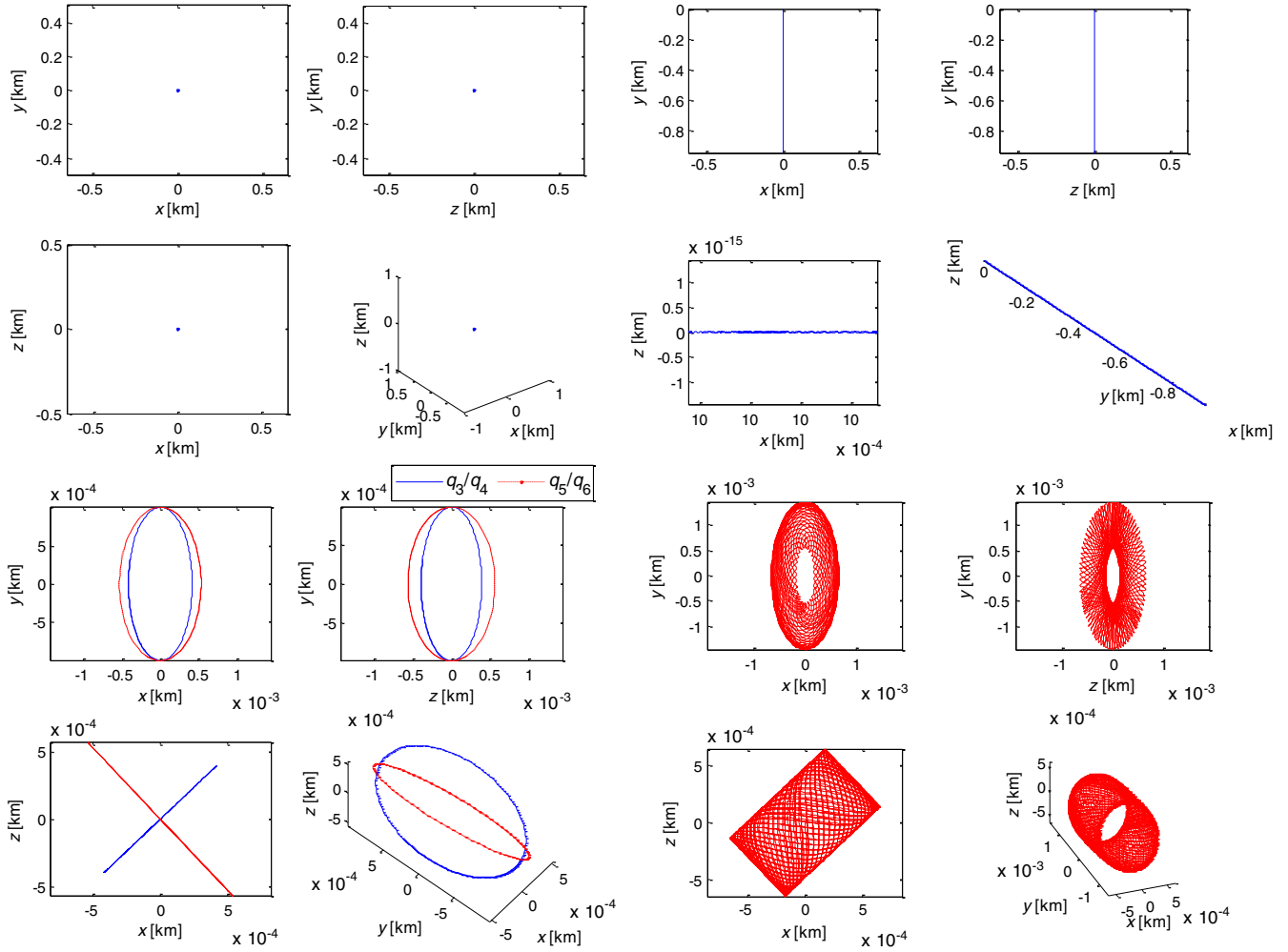
Fig. 4 Relationship between the natural frequencies and the displaced height: (a) the relationship among ω_2, ω_3, and h; (b) the relationship between ω_3/ω_2 and h.

Eq. (18) is easy to verify, i.e., $\Delta x = \Delta z = 0$, $\Delta y \neq 0$, $\Delta \dot{x} = \Delta \dot{y} = \Delta \dot{z} = 0$, which is substituted into Eq. (16) or Eq. (18) to yield

$$-\omega^2 + \mu/r^3 = a \sin \alpha/\rho. \qquad (20)$$

It is interesting to prove that Eq. (20) can be derived from a and α in Eqs. (2) and (3). Thus, $\mathbf{q}_1 = [0, 1, 0, 0, 0, 0]^T$ is one of the eigenvectors of $\mathbf{\Phi}$ or $\tilde{\mathbf{\Phi}}$ and is derived from $\dot{\mathbf{X}} = \frac{d}{dt}[\Delta \mathbf{r}_o^T \quad \Delta \dot{\mathbf{r}}_o^T]^T = \mathbf{\Phi}\mathbf{X}$ or $\dot{\mathbf{X}} = \frac{d}{dt}[\Delta \mathbf{r}^T \quad \Delta \dot{\mathbf{r}}^T]^T = \tilde{\mathbf{\Phi}}\mathbf{X}$, where

$$\mathbf{\Phi} = \begin{bmatrix} \mathbf{0} & \mathbf{I} \\ -\mathbf{B} & -\mathbf{A} \end{bmatrix}, \qquad \tilde{\mathbf{\Phi}} = \begin{bmatrix} \mathbf{0} & \mathbf{I} \\ -\tilde{\mathbf{B}} & -\tilde{\mathbf{A}} \end{bmatrix}. \qquad (21)$$

According to the Jordan decomposition, the double zero eigenvalues have a geometric multiplicity of 1 but an algebraic multiplicity of 2. Thus, $\mathbf{\Phi}$ (or $\tilde{\mathbf{\Phi}}$) has the following Jordan decomposition

Fig. 5 Relative fundamental motions in the O_2 frame: the height, the radius, and the angular velocity of the displaced circular orbit are 150 km, r_{GEO}, and ω_{GEO}, respectively.
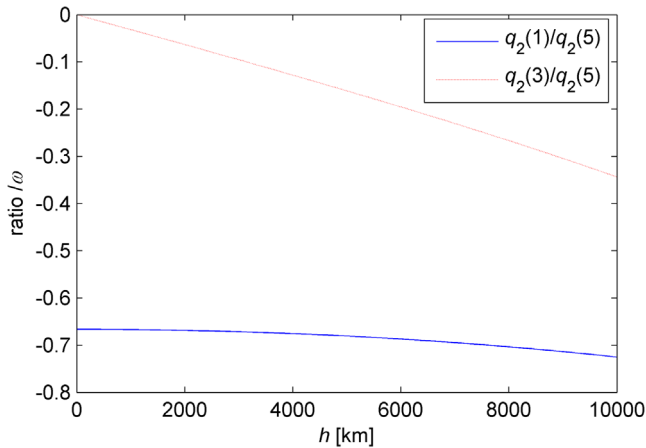

Fig. 6 Relationship between the displaced fundamental motions in the O_2 frame: the radius and the angular velocity of the displaced circular orbit are r_{GEO} and ω_{GEO}, respectively.

$$\begin{cases} x(t) = \left[4x_0 + \frac{2\dot{x}_0}{\omega}\right] + \frac{\dot{x}_0}{\omega} \sin \omega t - \left[3x_0 + \frac{2\dot{y}_0}{\omega}\right] \cos \omega t \\ y(t) = \left[y_0 - \frac{2\dot{x}_0}{\omega}\right] - 3[2\omega x_0 + \dot{y}_0]t + -2\left[3x_0 + \frac{2\dot{y}_0}{\omega}\right] \sin \omega t \\ \qquad + \frac{2\dot{x}_0}{\omega} \cos \omega t \\ z(t) = \frac{\dot{z}_0}{\omega} \sin \omega t + z_0 \cos \omega t \end{cases}$$

$$(25)$$

The third and fourth motions propagated from $\mathbf{q}_3$ and $\mathbf{q}_4$ show the same trajectories in the position space but have a different phase angle of $\pi/2$, shown as the blue trajectories in Fig. 5(c). From the linearized point of view, they are planar and periodic with the frequency of ω_2 and always hold the invariant momentum moment $\mathbf{H}_o = \Delta \mathbf{r}_o \times \Delta \dot{\mathbf{r}}_o$ (or $\mathbf{H} = \Delta \mathbf{r} \times \Delta \dot{\mathbf{r}}$). The same conclusion is obtained for the fifth and sixth motions propagated from $\mathbf{q}_5$ and $\mathbf{q}_6$ but with the circular frequency of ω_3, shown as the red trajectories in Fig. 5(c). The two momentum moments achieved by $\mathbf{q}_3/\mathbf{q}_4$ and $\mathbf{q}_5/\mathbf{q}_6$ are perpendicular to each other. In contrast to the single frequency periodic trajectories for the C-W equations, the general bounded relative trajectories remain on an invariant torus with the two frequencies ω_2 and ω_3 on the perpendicular axes, as shown in Fig. 5(d).

The structural stability of the relative trajectories at different displaced heights h should be verified. The 1:1 resonance case at
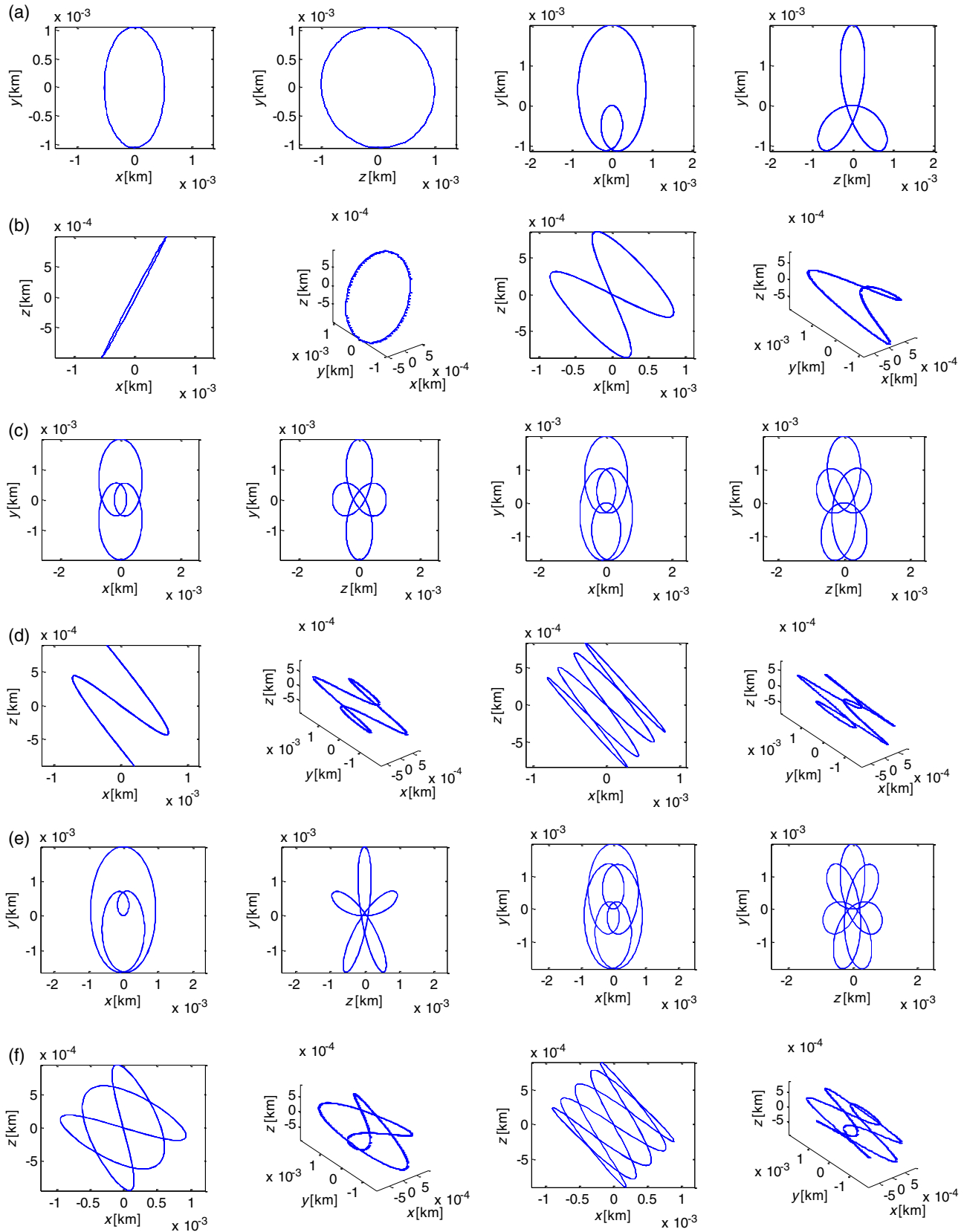
Fig. 7 Resonant relative trajectories in the cases in the $\mathbf{O}_2$ frame: (a) $\omega_2{:}\omega_3 = 1{:}1$, (b) $\omega_2{:}\omega_3 = 1{:}2$, (c) $\omega_2{:}\omega_3 = 1{:}3$, (d) $\omega_2{:}\omega_3 = 1{:}4$, (e) $\omega_2{:}\omega_3 = 2{:}3$, and (f) $\omega_2{:}\omega_3 = 2{:}5$.

$h = 0$, i.e., the classic C-W equations on the Keplerian circular orbit, has three double eigenvalues: 0, $+\omega$, and $-\omega$. The geometric multiplicity and algebraic multiplicity of $+\omega$ and $-\omega$ are two, respectively, which indicates that the $h = 0$ case has the same topological structure as the $h < h_{cri}$ cases. In the interval of $h \in [0, h_{cri})$, the ratio of ω_3/ω_2 increases from one to infinity, thus some rational ratios are available, i.e., the resonance cases $\omega_2 : \omega_3 = m : n$, where m and n are positive commutative integers. Then, all bounded relative trajectories will be periodic rather than quasiperiodic with orbital periods of $n \cdot 2\pi/\omega_2$ (or $m \cdot 2\pi/\omega_3$), as shown in Fig. 7, where the radius and the angular velocity of the displaced circular orbit are r_{GEO} and ω_{GEO}, respectively, and all trajectories are propagated from $\mathbf{q}_3 + \mathbf{q}_5$.

However, a bifurcation occurs at $h = h_{cri}$ where quadruple zero eigenvalues exist due to the degeneration of $\pm\omega_2$ into double zeros. The zero eigenvalues have an algebraic multiplicity of four and a geometric multiplicity of two with the Jordan norm form as $\mathbf{J}_1$ in Eq. (26) rather than the form as $\mathbf{J}_2$, which can be confirmed by the numerical results that all the eigenvalues of Φ^2 are real rather than Φ^4,

$$\mathbf{J}_1 = \begin{bmatrix} 0 & 1 & & & & \\ & 0 & & & & \\ & & 0 & 1 & & \\ & & 0 & 0 & & \\ & & & & 0 & -\omega_3 \\ & & & & \omega_3 & 0 \end{bmatrix},$$

$$\mathbf{J}_2 = \begin{bmatrix} 0 & 1 & & & & \\ & 0 & 1 & & & \\ & & 0 & 1 & & \\ & & & 0 & & \\ & & & & 0 & -\omega_3 \\ & & & & \omega_3 & 0 \end{bmatrix}. \tag{26}$$
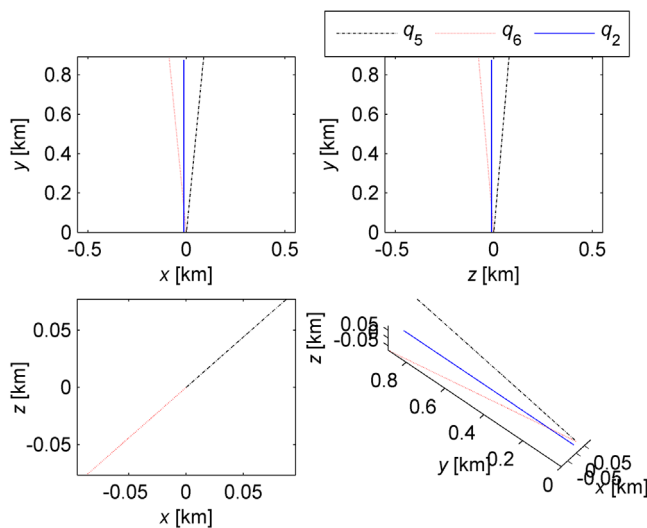
Four fundamental motions are solved from the Jordan decomposition, as $\mathbf{q}_1 = [0, 1, 0, 0, 0, 0]^T$ for the static station-keeping in the along-track direction, $\mathbf{q}_2 = [x_0 \quad 0 \quad z_0 \quad 0 \quad \dot{y}_0 \quad 0]^T$ provides the along-track velocity leaving or approaching the chief, and $\mathbf{q}_3/\mathbf{q}_4$ (with a difference in phase angle of $\pi/4$) provides the periodic trajectories with the only frequency of ω_3.

For the $h > h_{cri}$ case, the double zero eigenvalues with the geometric multiplicity of one cause the two fundamental motions propagated from $\mathbf{q}_1$ and $\mathbf{q}_2$, and the conjugate imaginary eigenvalues provide the periodic trajectories with the only frequency of ω_3 propagated from $\mathbf{q}_3$ and $\mathbf{q}_4$. The real eigenvalues $\pm\lambda$ generate the unstable $e^{\pm\lambda_t} \approx 1 \pm \lambda t$ terms, which causes the other leaving (or approaching) directions to propagate from their eigenvectors $\mathbf{q}_5$ and $\mathbf{q}_6$ (they have the same components, with the exception of the opposite y_0 and $\dot{y}_0$ components), as shown in Fig. 8. The results indicate that $\mathbf{q}_2$, $\mathbf{q}_5$, and $\mathbf{q}_6$ are independent of each other.

3.3 Off-Axis Equilibrium by Extracontrol

In the previous discussion, all equilibria solved from the linearized relative Eq. (16) are located in the along-track direction (i.e., y axis), which is referred to as the along-axis equilibrium. However, some astronautical missions, such as the phased array antenna in Sec. 5, require the centers of relative tori to be located above or behind the y axis, which is referred to as the off-axis equilibrium and denoted as $\Delta\mathbf{r}_* = [\Delta x_*, \Delta y_*, \Delta z_*]^T$.

The new relative position of the follower with respect to the off-axis equilibrium is denoted by $\delta\mathbf{r} = \Delta\mathbf{r}_0 - \Delta\mathbf{r}_*$; it is substituted into Eq. (16) to yield

$$\delta\ddot{\mathbf{r}} + \mathbf{A}\delta\dot{\mathbf{r}} + \mathbf{B}\delta\mathbf{r} = \mathbf{u}_o - \mathbf{B}\Delta\mathbf{r}^*. \tag{27}$$

If the extracontrol of the follower $\mathbf{u}_o$ is set as the open-loop $\mathbf{u}_o = \mathbf{B}\Delta\mathbf{r}_*$ in the $\mathbf{O}$ frame, Eq. (27) will degenerate into Eq. (16), which indicates that both the numerical and analytical solutions developed in Secs. 3.2 and 4.1 are available for the off-axis equilibrium case. An illustration of the off-axis periodic relative trajectories is shown in Fig. 9, where the height, the radius, and the angular velocity of the displaced circular orbit are 150 km, r_{GEO}, and ω_{GEO}, respectively. Rather than periodic trajectories from
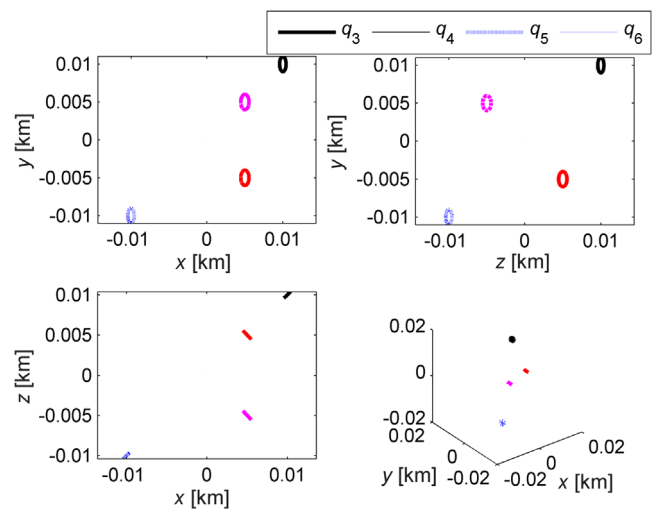

Fig. 8 Unbounded relative trajectories propagated from q_2 and q_5 in the cases in the $\mathbf{O}_2$ frame: the height, the radius, and the angular velocity of the displaced circular orbit are 19,000 km, r_{GEO}, and ω_{GEO}, respectively.

Fig. 9 Off-axis relative trajectories propagated from q_3, q_4, q_5, and q_6 in the $\mathbf{O}$ frame: (a) black trajectory, $\Delta\mathbf{r}_* = [1, 1, 1]^T$ km; (b) red trajectory, $\Delta\mathbf{r}_* = [0.5, -0.5, 0.5]^T$ km; (c) blue trajectory, $\Delta\mathbf{r}_* = [-1, -1, -1]^T$ km; and (d) magenta trajectory, $\Delta\mathbf{r}_* = [0.5, 0.5, -0.5]^T$ km.

$\mathbf{q}_3$, $\mathbf{q}_4$, $\mathbf{q}_5$, and $\mathbf{q}_6$, some fixed points propagated from $\mathbf{q}_1$ will maintain a constant distance and orientation in space, which has potential applications in InSAR measurement on a displaced GEO.

Thus, the expected acceleration of the follower provided by the low thrust is given in the chief-centered $\mathbf{O}$ frame as

$$\mathbf{u}_o = \mathbf{B}\Delta\mathbf{r}^* + \begin{bmatrix} \cos(\theta - \alpha) \\ 0 \\ \sin(\theta - \alpha) \end{bmatrix} - \begin{bmatrix} 0 \\ a\,\sin\alpha \cdot \Delta\varphi \\ 0 \end{bmatrix}, \qquad (28)$$

where the first term is the extracontrol, the second term is the BPA of the chief, and the third term is the difference in BPA between the follower and the chief.

4 Linearized Relative Motions in a Displaced Circular Orbit Derived from Reduced Dynamics

4.1 Linearized Relative Motions Derived from Reduced Dynamics and Their Analytical Solutions

In the reduced dynamics, the displaced circular orbit of the chief is mapped onto an equilibrium point in the (ρ, h) space, which is denoted by ρ_0, h_0, and ϕ_0 ($=\omega t$, i.e., the angular momentum along the z_i axis (MMZA) $h_{z0} = \rho_0^2 \cdot \omega$) in the $\mathbf{C}$ frame. With only the BPA, the moment of momentum along the z_i axis will always remain invariant. However, the follower may have a different angular momentum denoted $h_z = h_{z0} + \Delta h_z$, with the angular component denoted $\phi = \phi_0 + \Delta\phi$.

To derive the follower's linearized relative motions with respect to the chief, an intermediate orbit (ρ_1, h_1), which is defined as the displaced circular orbit with the same h_z as the follower's one, is introduced in this section. (ρ_1, h_1) is the equilibrium of Eq. (5), and $\delta\rho = \rho_1 - \rho_0$ and $\delta h = h_1 - h_0$ have the following relationship between chief's (ρ_0, h_0) and Δh_z by the Taylor linearization as

$$\begin{cases} \left(3\mu\frac{h_{z0}^2}{\rho_0^4} - 3\mu\frac{\rho_0^2}{r_0^5} + \frac{\mu}{r_0^3}\right)\delta\rho - 3\mu\frac{\rho_0 h_0}{r_0^5}\delta h = 2\mu\frac{h_{z0}}{\rho_0^3}\Delta h_z \\ \left(\frac{1}{h_0} - 3\frac{h_0}{r_0^2}\right)\delta h - 3\frac{\rho_0}{r_0^2}\delta\rho = 0 \end{cases}, \qquad (29)$$

where $r_0 = \sqrt{\rho_0^2 + h_0^2}$. Thus, both $\delta\rho$ and δh can be solved from the previous equation and are dependent on Δh_z but independent of time.

Compared with the intermediate orbit, the position components of the follower are denoted by $\rho = \rho_1 + \Delta\rho$, $h = h_1 + \Delta h$; they are substituted into Eqs. (5) and (6) to simplify the equation by the Taylor linearization, which yields

$$\begin{bmatrix} \Delta\ddot{\rho} \\ \Delta\ddot{h} \end{bmatrix} = \mathbf{M}\begin{bmatrix} \Delta\rho \\ \Delta h \end{bmatrix},$$

$$\mathbf{M} = \begin{bmatrix} -3\frac{h_z^2}{\rho_1^4} + 3\mu\frac{\rho_1^2}{r_1^5} - \frac{\mu}{r_1^3} & 3\mu\frac{\rho_1 h_1}{r_1^5} \\ 3\mu\frac{\rho_1 h_1}{r_1^5} & 3\mu\frac{h_1^2}{r_1^5} - \frac{\mu}{r_1^3} \end{bmatrix}, \qquad (30)$$

but the angular component is simplified compared with chief as

$$\Delta\ddot{\phi} = -2\frac{\omega}{\rho_0}(\Delta\dot{\rho} + \delta\dot{\rho}) = -2\frac{\omega}{\rho_0}\Delta\dot{\rho}, \qquad (31)$$

where $h_z = h_{z0} + \Delta h_z$, $r_1 = \sqrt{\rho_1^2 + h_1^2}$. Equation (30) does not have a velocity term, which greatly contributes to deriving the analytical solutions of Eqs. (30) and (31). Therefore, a real nonsingular matrix $\mathbf{T}$ exists to transform $\mathbf{M}$ into a diagonal matrix by two eigenvalues η_1 and η_2, i.e., $\mathbf{T}^{-1}\mathbf{M}\mathbf{T} = \begin{bmatrix} \eta_1 & 0 \\ 0 & \eta_2 \end{bmatrix}$, where

$$\eta_1 = \mu\left(\frac{1}{2r_1^3} - \frac{3}{2\rho_1^3} - \frac{3}{2}\sqrt{\left(\frac{1}{\rho_1^3} + \frac{1}{r_1^3}\right)^2 - \frac{4}{\rho_1 r_1^5}}\right),$$

$$\eta_2 = \mu\left(\frac{1}{2r_1^3} - \frac{3}{2\rho_1^3} + \frac{3}{2}\sqrt{\left(\frac{1}{\rho_1^3} + \frac{1}{r_1^3}\right)^2 - \frac{4}{\rho_1 r_1^5}}\right), \qquad (32)$$

$$\mathbf{T} = \begin{bmatrix} \dfrac{3\mu\rho_1 h_1}{r_1^5} & \dfrac{-3\mu(r_1^2\rho_1^3 + r_1^5 - 2\rho_1^5)}{2r_1^5\rho_1^3} + \dfrac{3\mu}{2}\sqrt{\left(\frac{1}{\rho_1^3} + \frac{1}{r_1^3}\right)^2 - \frac{4}{\rho_1 r_1^5}} \\ \dfrac{3\mu(r_1^2\rho_1^3 + r_1^5 - 2\rho_1^5)}{2r_1^5\rho_1^3} - \dfrac{3\mu}{2}\sqrt{\left(\frac{1}{\rho_1^3} + \frac{1}{r_1^3}\right)^2 - \frac{4}{\rho_1 r_1^5}} & \dfrac{3\mu\rho_1 h_1}{r_1^5} \end{bmatrix}. \qquad (33)$$

Furthermore, some discussions about η_1 and η_2 are listed as follows:

a. when $h_1 = 0$, both eigenvalues are negative and equal as $\eta_1 = \eta_2 = -\frac{\mu}{\rho_1^3}$; they are denoted by the pair $-\omega_2^2$ and $-\omega_2^2$ ($\omega_2 > 0$, $\omega_3 = \omega_2$), respectively;

b. when $0 < h_1 < h_{\text{cri}} = \rho_0\sqrt{\sqrt[3]{\frac{1}{8}\left(1 - \rho_1^2\frac{4\mu^2}{9h_z^2}\right) + \sqrt{\frac{1}{64}\left(1 - \rho_1^2\frac{4\mu^2}{9h_z^2}\right)^2 - \frac{1}{64}}} - \sqrt[3]{\frac{1}{8}\left(1 - \rho_1^2\frac{4\mu^2}{9h_z^2}\right) - \sqrt{\frac{1}{64}\left(1 - \rho_1^2\frac{4\mu^2}{9h_z^2}\right)^2 - \frac{1}{64}}}}$ (for the displaced GEO with $\rho_1 = r_{\text{GEO}}$ and $\omega = \omega_{\text{GEO}}$, h_{cri} is equal to 18,700 km), the two eigenvalues are negative and different; they are denoted by $-\omega_2^2$ and $-\omega_3^2$ ($0 < \omega_2 < \omega_3$), respectively;

c. when $h_1 = h_{\text{cri}}$, one of the eigenvalues is equal to zero, and the other eigenvalue is negative; they are denoted by 0 and $-\omega_3^2$ ($\omega_3 > 0$, $\lambda = 0$), respectively;

d. when $h_1 > h_{\text{cri}}$, one of the eigenvalues is positive, and the other is negative; they are denoted by $+\lambda^2$ and $-\omega_3^2$ ($\lambda > 0$, $\omega_3 > 0$), respectively.

Considering the geometry of the $\mathbf{C}$ and $\mathbf{O}_2$ frames, it is derived by a first-order approximation

$$\begin{cases} \Delta x = \rho \cos \Delta\phi - \rho_0 \approx \Delta\rho + \delta\rho \\ \Delta y = \rho \sin \Delta\phi \approx \rho_0 \Delta\varphi \\ \Delta z = \Delta h + \delta h \end{cases}, \qquad (34)$$

which indicates that the two frames are equal, and the analytical solutions to Eq. (16) or Eq. (18) can be derived from Eqs. (29)–(31) as

$$\text{when } h_1 < h_{\text{cri}}, \begin{cases} \Delta x = \mathbf{T}_{11} \cdot a_2 \cos(\omega_2 t + b_2) + \mathbf{T}_{12} \cdot a_3 \cos(\omega_3 t + b_3) + \delta\rho \\ \Delta y = \rho_0 \Delta\phi|_0 + \mathbf{T}_{11} \cdot a_2 \frac{2\omega}{\omega_2} \sin b_2 + \mathbf{T}_{12} \cdot a_3 \frac{2\omega}{\omega_2} \sin b_3 + (\rho_0 \Delta\dot\phi|_0 + \mathbf{T}_{11} \cdot a_2 2\omega \cos b_2 + \mathbf{T}_{12} \cdot a_3 2\omega \cos b_3)t \\ \quad -\mathbf{T}_{11} \cdot a_2 \frac{2\omega}{\omega_2} \sin(\omega_2 t + b_2) - \mathbf{T}_{12} \cdot a_3 \frac{2\omega}{\omega_3} \sin(\omega_3 t + b_3) \\ \Delta z = \mathbf{T}_{21} \cdot a_2 \cos(\omega_2 t + b_2) + \mathbf{T}_{22} \cdot a_3 \cos(\omega_3 t + b_3) + \delta h \end{cases}, \qquad (35)$$

$$\text{when } h_1 = h_{\text{cri}}, \begin{cases} \Delta x = \mathbf{T}_{11} \cdot (a_2 + b_2 t) + \mathbf{T}_{12} \cdot a_3 \cos(\omega_3 t + b_3) + \delta\rho \\ \Delta y = \rho_0 \Delta\phi|_0 + \mathbf{T}_{12} \cdot a_3 \frac{2\omega}{\omega_2} \sin b_3 + (\rho_0 \Delta\dot\phi|_0 + \mathbf{T}_{12} \cdot a_3 2\omega \cos b_3)t - \mathbf{T}_{11} \cdot \omega b_2 t^2 - \mathbf{T}_{12} \cdot a_3 \frac{2\omega}{\omega_3} \sin(\omega_3 t + b_3) \\ \Delta z = \mathbf{T}_{21} \cdot (a_2 + b_2 t) + \mathbf{T}_{22} \cdot a_3 \cos(\omega_3 t + b_3) + \delta h \end{cases}, \qquad (36)$$

$$\text{when } h_1 > h_{\text{cri}}, \begin{cases} \Delta x = \mathbf{T}_{11} \cdot (a_2 e^{\lambda t} + b_2 e^{-\lambda t}) + \mathbf{T}_{12} \cdot a_3 \cos(\omega_3 t + b_3) + \delta\rho \\ \Delta y = \rho_0 \Delta\phi|_0 + \mathbf{T}_{11} \cdot \frac{2\omega}{\lambda}(a_2 - b_2) + \mathbf{T}_{12} \cdot a_3 \frac{2\omega}{\omega_2} \sin b_3 + [\rho_0 \Delta\dot\phi|_0 + \mathbf{T}_{11} \cdot 2\omega(a_2 + b_2) + \mathbf{T}_{12} \cdot a_3 2\omega \cos b_3]t \\ \quad -\mathbf{T}_{11} \cdot \frac{2\omega}{\lambda}(a_2 e^{\lambda t} - b_2 e^{-\lambda t}) - \mathbf{T}_{12} \cdot a_3 \frac{2\omega}{\omega_3} \sin(\omega_3 t + b_3) \\ \Delta z = \mathbf{T}_{21} \cdot (a_2 e^{\lambda t} + b_2 e^{-\lambda t}) + \mathbf{T}_{22} \cdot a_3 \cos(\omega_3 t + b_3) + \delta h \end{cases}, \qquad (37)$$

where $\mathbf{T}_{ij}$ is the element in the i'th row and the j'th column of $\mathbf{T}$, $\Delta\phi_0$ and $\Delta\dot\phi_0$ are determined by the initial value and its velocity at the epoch moment, and a_m, b_n $(m, n) = (2,3)$ is determined as

$$\text{when } h_1 < h_{\text{cri}}, \begin{bmatrix} a_2 \cos b_2 \\ a_3 \cos b_3 \end{bmatrix} = \mathbf{T}^{-1} \begin{bmatrix} \Delta x|_0 - \delta\rho \\ \Delta z|_0 - \delta h \end{bmatrix}, \quad \text{and} \quad \begin{bmatrix} a_2 \sin b_2 \\ a_3 \sin b_3 \end{bmatrix} = \begin{bmatrix} 1/\omega_2 & 0 \\ 0 & 1/\omega_3 \end{bmatrix} \mathbf{T}^{-1} \begin{bmatrix} \Delta\dot x|_0 \\ \Delta\dot z|_0 \end{bmatrix}, \qquad (38)$$

$$\text{when } h_1 = h_{\text{cri}}, \begin{bmatrix} a_2 \\ a_3 \cos b_3 \end{bmatrix} = \mathbf{T}^{-1} \begin{bmatrix} \Delta x|_0 - \delta\rho \\ \Delta z|_0 - \delta h \end{bmatrix}, \quad \text{and} \quad \begin{bmatrix} b_2 \\ a_3 \sin b_3 \end{bmatrix} = \begin{bmatrix} 1/\lambda & 0 \\ 0 & 1/\omega_3 \end{bmatrix} \mathbf{T}^{-1} \begin{bmatrix} \Delta\dot x|_0 \\ \Delta\dot z|_0 \end{bmatrix}, \qquad (39)$$

$$\text{when } h_1 > h_{\text{cri}}, \begin{bmatrix} a_2 + b_2 \\ a_3 \cos b_3 \end{bmatrix} = \mathbf{T}^{-1} \begin{bmatrix} \Delta x|_0 - \delta\rho \\ \Delta z|_0 - \delta h \end{bmatrix}, \quad \text{and} \quad \begin{bmatrix} a_2 - b_2 \\ a_3 \sin b_3 \end{bmatrix} = \begin{bmatrix} 1/\lambda & 0 \\ 0 & 1/\omega_3 \end{bmatrix} \mathbf{T}^{-1} \begin{bmatrix} \Delta\dot x|_0 \\ \Delta\dot z|_0 \end{bmatrix}. \qquad (40)$$

The difference in MMZA between the follower and the chief, i.e., Δh_z, can be achieved from the initial values. Substituting the initial $\rho = \rho_0 + \Delta\rho|_0 + \delta\rho = \rho_0 + \Delta x|_0$ and $\dot\phi = \omega + \Delta\dot\phi|_0$ into $h_z = \rho^2 \dot\phi$ and simplifying by the Taylor linearization yields

$$\Delta h_z = 2\frac{\Delta x|_0}{\rho_0} + \frac{\Delta\dot\phi|_0}{\omega}. \qquad (41)$$

Therefore, combining Eqs. (29) and (35)–(41) yields the analytical solutions to the linearized relative motions. Figure 10 is the comparison between the numerical solutions and analytical solutions, which confirms that Eqs. (16), (18), (30), and (31) are equivalent. Some discussions about the analytical results are listed as follows:

a. the results prove that the analytical solutions will degenerate into Eq. (25) when $h_1 = 0$;

b. when $h_1 < h_{\text{cri}}$, the only factor that causes the boundedness in the along-track direction is the zero initial value of $\Delta\dot\phi|_0 + \mathbf{T}_{11} \cdot a_2 \frac{2\omega}{\rho_0} \cos b_2 + \mathbf{T}_{12} \cdot a_3 \frac{2\omega}{\rho_0} \cos b_3 = 0$ or $\Delta\dot\phi|_0 + \mathbf{T}_{11} \cdot \frac{2\omega}{\rho_0}(a_2 + b_2) + \mathbf{T}_{12} \cdot a_3 \frac{2\omega}{\rho_0} \cos b_3 = 0$, which will degenerate into the C-W "zero" condition as $\Delta\dot\phi|_0 + \frac{2\omega}{\rho_0} \Delta x|_0 = 0$. The relative trajectories that satisfy the condition are referred to as the naturally bounded trajectories.

4.2 Bounded Relative Trajectories by Extracontrol

In general, science applications based on formation flying require the spacecraft to remain in the vicinity of each other. However, a slight deviation from the initial values (e.g., $\mathbf{q}_3, \ldots, \mathbf{q}_6$ or $\Delta\dot\phi_0 = 0$ when $h_0 < h_{\text{cri}}$) generates an increase over time in the along-track component. Thus, controlled
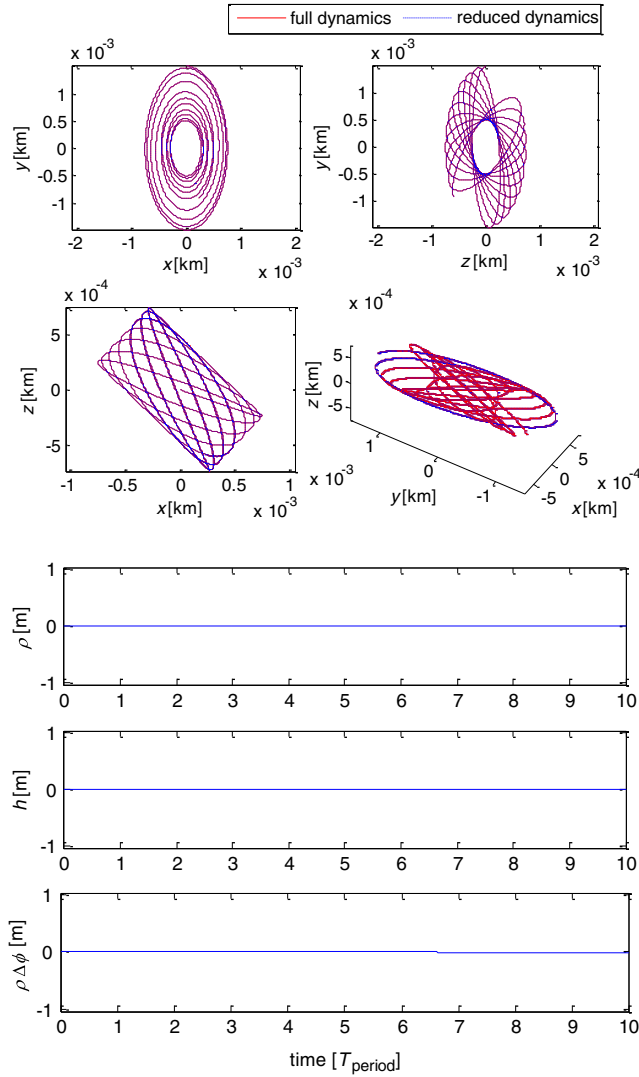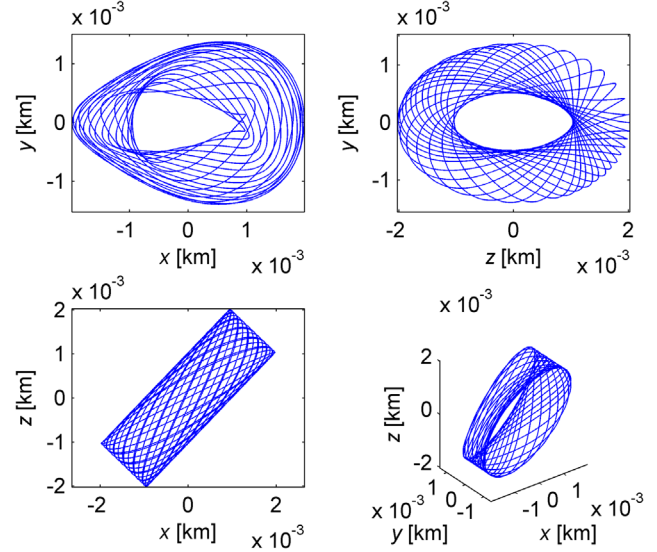
Fig. 11 Bounded controlled relative trajectories regardless of the initial values when $h_0 < h_{cri}$ integrated in the nonlinear relative dynamics and drawn in the $\mathbf{O}_2$ frame: the height, the radius, and the angular velocity of the displaced circular orbit are 150 km, r_{GEO}, and ω_{GEO}, respectively; the control parameters ω_1 and δ are $2\omega_{GEO}$ and 1×10^{-6}.

$$\Delta\phi = a_1 \sin(\omega_1 t + b_1) + \frac{\mathbf{T}_{11} \cdot a_2\omega_2}{\omega_1^2 - \omega_2^2} \sin(\omega_2 t + b_2)$$
$$+ \frac{\mathbf{T}_{12} \cdot a_3\omega_3}{\omega_1^2 - \omega_3^2} \sin(\omega_3 t + b_3), \tag{43}$$

where a_1 and b_1 are determined by the initial values at the epoch moment. The new frequency ω_1 is equal to neither ω_2 nor ω_3 to avoid resonance. To make the proposed control available in the nonlinear relative dynamics, a very small damping term $\delta\Delta\dot\phi$ is added as $u = -\omega_1^2\Delta\phi - \delta\Delta\dot\phi$ to maintain the controlled poles away from the imaging axis, as shown in Fig. 11.

When $h_0 \geq h_{cri}$, the stabilization in the $\Delta\phi$ (or Δy) direction is implemented by the same controller as the $h_0 < h_{cri}$ case; however, the real eigenvalues $\pm\lambda$ along the other directions can be stabilized by the Hamiltonian-structure control (HSP). HSP is a sufficiently powerful tool to stabilize motions near the unstable equilibrium, which is developed by Refs. 21–23. Due to the Hamiltonian structure of dynamics in the (ρ, h) space, i.e., $\begin{cases} \ddot\rho = -\partial\overline{U}/\partial\rho \\ \ddot{h} = -\partial\overline{U}/\partial h \end{cases}$, where $\overline{U} = U + h_z^2/2\rho^2$, the HSP can be designed as

$$\mathbf{u} = -[G_1 \cdot \lambda^2(\mathbf{v}_+\mathbf{v}_+^T + \mathbf{v}_-\mathbf{v}_-^T) + G_2 \cdot \omega_3^2(\mathbf{v}\mathbf{v}^H + \overline{\mathbf{v}}\,\overline{\mathbf{v}}^H)]$$
$$\cdot [\Delta\rho \quad \Delta h]^T - \varpi\mathbf{J} \cdot [\Delta\dot\rho \quad \Delta\dot{h}]^T, \tag{44}$$

where $\mathbf{J}$ is the symplectic matrix; G_1 and G_2 are the control gains; ϖ is the gain of the Coriolis term; $\mathbf{v}_+$ and $\mathbf{v}_-$ are the eigenvectors that correspond to the real eigenvalues $+\lambda$ and $-\lambda$, respectively; and $\mathbf{v}$ and $\overline{\mathbf{v}}$ are the conjugate eigenvectors that correspond to the imaginary eigenvalues $\pm\omega_3$. In the controller, the G_1 term is used to weaken the unstable manifolds characterized by $+\lambda$, the G_2 term is used to strengthen the center manifolds characterized by $\pm\omega_3$, and the ϖ term is used to strengthen the coupling effects of the previous two terms. The controlled bounded trajectories are shown in Fig. 12 regardless of the initial values.
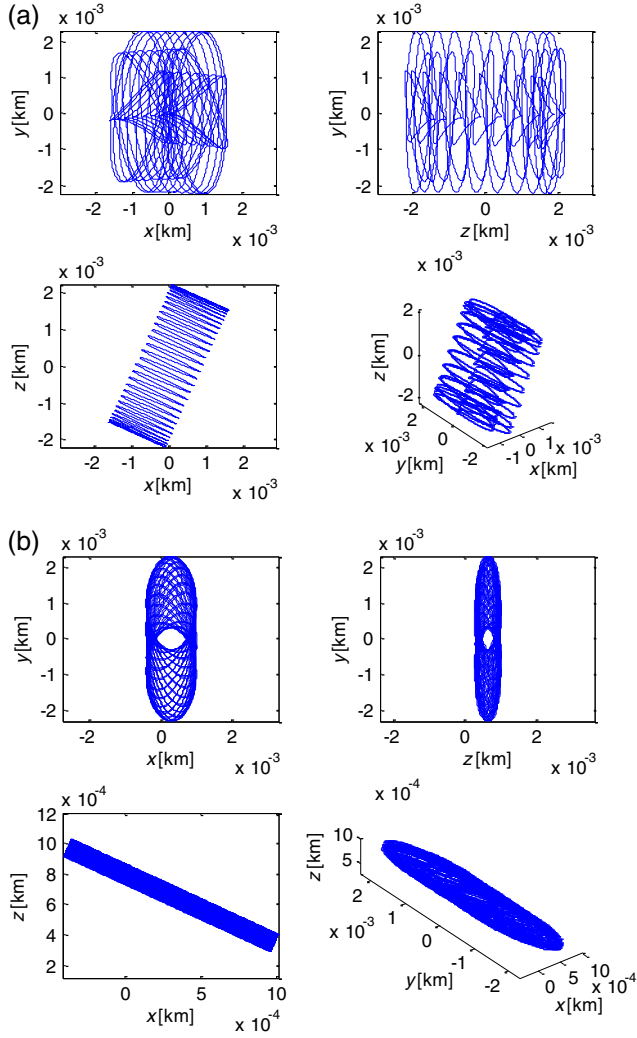

Fig. 10 Comparison between the numerical integration of linearized equations from spatial dynamics and the analytical solution of the linearized equation of the reduced dynamics in the $\mathbf{O}_2$ frame: the height, the radius, and the angular velocity of the displaced circular orbit are 150 km, r_{GEO}, and ω_{GEO}, respectively.

bounded relative trajectories with the arbitrary initial values are investigated in this section. In practice, the low-thrust propulsion used by the follower can supply the BPA to displace above the Earth and the extra-acceleration to generate bounded trajectories for any initial value.

When $h_0 < h_{cri}$, Eqs. (35)–(37) demonstrate that the motions along the $\Delta\rho$ (or Δx) and Δh (or Δz) directions are always bounded, with the exception of the $\Delta\phi$ (or Δy). Thus, a closed-loop control with only the feedback from $\Delta\phi$, i.e., $u = -\omega_1^2\Delta\phi$, is proposed in this section to yield this new type of relative trajectories, which is formulized as

$$\Delta\ddot\phi = -2\frac{\omega}{\rho_0}\Delta\dot\rho + u, \tag{42}$$

where $\Delta\dot\rho = -\mathbf{T}_{11} \cdot a_2\omega_2 \sin(\omega_2 t + b_2) - \mathbf{T}_{12} \cdot a_3\omega_3 \sin(\omega_3 t + b_3)$ is derived from Eq. (35). Thus, the extracontrol $\mathbf{u} = [0; u; 0]^T$ of the follower introduces a new frequency ω_1 in the along-track direction, which is indicated by the analytical solutions to Eq. (42) as

Fig. 12 Bounded controlled relative trajectories regardless of the initial values: (a) when $h_0 > h_{cri}$; (b) when $h_0 = h_{cri}$ integrated in the nonlinear relative dynamics and drawn in the O_2 frame; the height, the radius, and the angular velocity of the displaced circular orbit are 19,000 km (a) or h_{cri} (b), r_{GEO} and ω_{GEO}, respectively; the control parameters ω_1, δ, and (G_1, G_2, ϖ) are $2\omega_{GEO}$, 1×10^{-7} and (1,0,0) for (a) or (0,1, 1×10^{-7}) for (b).

5 Applications in a Displaced Geostationary Orbit Mission

A cluster on a displaced orbit has a range of potential applications, such as Earth surface imaging and cooperative communication. Here, two examples are provided for a displaced GEO: the first example is to fix the relative baseline vector for InSAR measurement or Earth imaging by a chief and a follower, and the second example is to provide repeating relative ground tracks for space-based phased array antenna missions.

5.1 Fixed Relative Baseline Vector for InSAR or Fresnel Zone Lens Missions

InSAR systems could generate high-resolution radar images of Earth's surface using the amplitude and phase information of received echoes in any weather or lighting conditions.[24] Different receiver configurations can be used to produce digital elevation models (DEM), detect moving objects on the

ground, produce super-resolution imagery, or measure temporally changing terrain features. Usually, a certain line-of-sight angle (defined as the angle between the line of sight and the z_o axis) or beam angle from the cluster to the target prefers a fixed pointing direction. To minimize the measuring errors, the optimal length of the across-track baseline for DEM can be calculated, which is dependent on the beam angle of the radar equipment.

According to Ref. 25, the across-track baseline B^n is the component normal to the sight-line of the projection of the spatial baseline **B** onto the range-elevation plane, formulated as

$$B^n = B \cdot [\sin\theta_L \cos\theta_L \cos\gamma - \cos\theta_L \sin\gamma]^T, \quad (45)$$

where θ_L is the line-of-sight angle, γ is the squint-angle separated from orbital plane, and **B** is the baseline measuring the relative position of formation crafts. For the radar equipment in Ref. 25, the line-of-sight angle for DEM is set to $\theta_L = 35$ deg on the lower left side of the along-track direction, $\gamma = 90$ deg, and the length of the baseline is set to $B = 5$ km. To maximize B^n, the baseline **B** is designed parallel to $[\sin\theta_L \cos\theta_L \cos\gamma - \cos\theta_L \sin\gamma]^T$, thus the off-axis equilibrium $\Delta r_* = B[-\sin\theta_L, 0, \cos\theta_L]^T$ is designed according to the extra-control strategy developed in Sec. 3.3 to yield a fixed distance.

In this mission, the radar is installed on the chief and, assuming that there is an angle between the radar and the thrust direction, is denoted by ξ. To observe the Earth surface at different latitudes, the radar is required to rotate a certain angle to be perpendicular to the line-of-sight, which results in the variation of the thrust direction. Limited by the observing region and the thrust direction, the radius and displaced height of the chief's orbit can be determined uniquely. The sketch of the InSAR system and the orientation baseline provided by the follower and the chief are shown in Fig. 13(a). According to the spatial baseline, the relative motion and the orbit of the follower can be obtained as well. Some examples are presented below to show how the displaced formations apply to the observation of different latitudes of the Earth.

In the simulation, the orbit of the chief is displaced at the height of 150 km with $\rho = r_{GEO}$, $\omega = \omega_{GEO}$, which can observe the Earth surface around 0.2-deg latitude, and the thrust direction is approximately parallel to the radar (the installation angle ξ between the thrust direction and radar is 0.1 deg). The orbit of the follower is displaced at $h = 154$ km with $\rho = 42,161$ km, $\omega = \omega_{GEO}$ so that the initial conditions of the relative motions are $[\Delta r_*, 0, 0]^T$ in the chief's **O** frame. Compared with the BPA of 7.97×10^{-4} m/s² required by the chief, the required acceleration of the follower is 8.20×10^{-4} m/s². Considering an electric thruster with a specific impulse of 3000 s and a large 1000 kg geostationary platform, for example, the extra-propellant mass per orbit (or day) for the follower is 0.05 kg. To observe another region of the Earth, for example, the surface around 5-deg latitude, the thrust direction of the chief is changed from -0.306 deg to -4.892 deg due to a constant $\xi = 0.1$ deg. With the angular velocity $\omega = \omega_{GEO}$, the height and radius of the displaced orbit are solved as $h = 3684$ km, $\rho = 42,108$ km. The relationships between the observation latitude δ and the location of the chief's displaced orbit under different installation angles ξ are shown in Fig. 13(b), which indicates the displaced height increases with the increasing latitude δ.

From the perspective of the interferometry, the optimal length of the across-track baseline is expected to remain
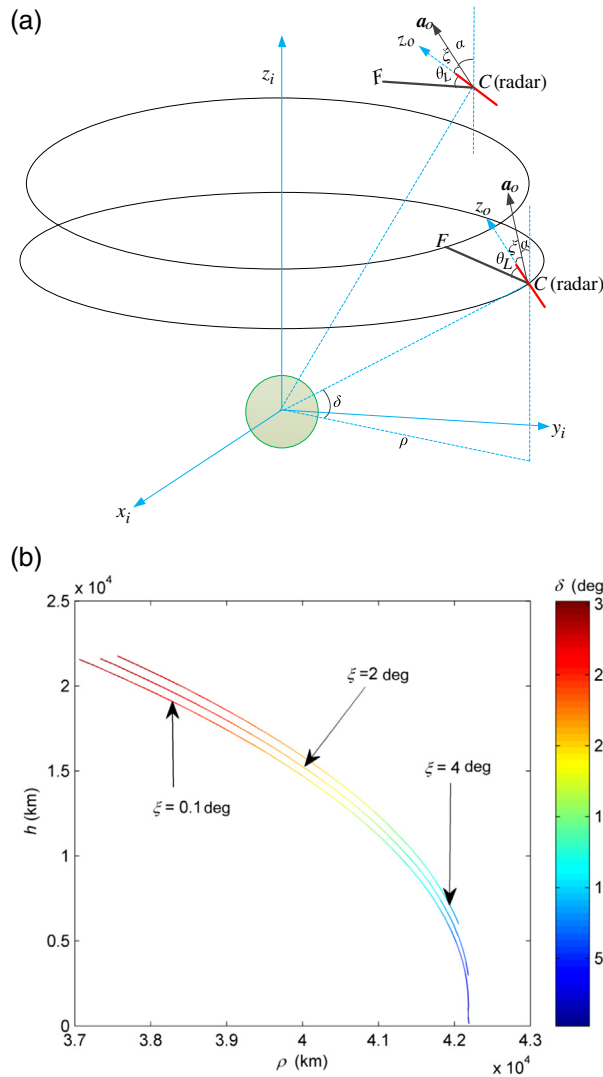
(a)

(b)

Fig. 13 Fixed relative baseline vector for the InSAR missions: (a) abridged general view of the geometry of the follower, the chief, and the fixed baseline; (b) relationships between the observation latitude δ and the location of the chief's displaced orbit under different installation angles ξ.

(a)

(b)

Fig. 14 Fixed relative baseline vector for the Fresnel zone lens missions: (a) abridged general view of the geometry of the follower, the chief, and the fixed baseline; (b) relationships between the angle η and the chief's displaced orbit for different observation latitudes δ; the installation angle between the thrust direction and lens is $\xi = 0.1$ deg.

unchanged for the entire orbital period, that is, the chief and follower stay parallel, then achieve the interferometry at any moment. However, the classic formation cannot realize the parallel relative motion, and the classic follower's configurations in the vicinity of the chief produce a sine-like wave-shaped baseline. It indicates that only two spacecraft in classic formation cannot provide a fixed baseline vector and only certain positions of the trajectories can be utilized for the InSAR mission.[26] The practice of the TSX-TDX mission developed by DLR also verifies the previous conclusion: a series of configurations were used in the mission life, as any configuration can work in a narrow range of geographical altitudes due to the time-dependent baseline.[27] On the contrary, the distributed situational observer in displaced orbits can easily form a parallel configuration, and the across-track baseline is fixed, which removes the restriction of interferometry in the position and time compared with the classical formation around Keplerian orbits.

For the Earth surface–chief–follower colinear case shown in Fig. 14(a), the chief and the follower can act as the Fresnel zone
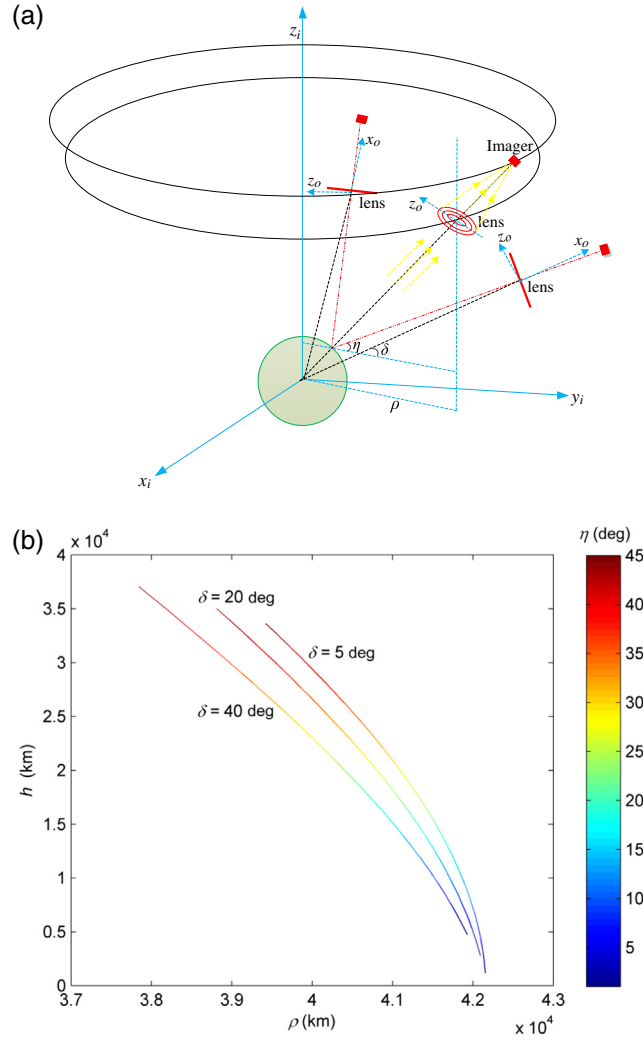
lens and the charge-coupled-device (CCD) imager, respectively, to create a space-based large distributed lens. The Fresnel zone lens is a focusing and imaging device with the lenses of large aperture and short focal length, which can capture more oblique light from a light source, thus allowing the light to be visible over greater distances.[28] Since the Fresnel zone lens and the CCD imager are widely used and investigated in the field of optical systems, this section merely discusses the application of displaced formation in the Earth surface imaging in terms of the trajectory design.

In this mission, the orbit of the chief (i.e., Fresnel zone lens) is still displaced at the height of 150 km with $\rho = r_{GEO}$, $\omega = \omega_{GEO}$, and the off-axis equilibrium lies along the x_o axis, as $\Delta \mathbf{r}* = f \cdot [1, 0, 0]^T$, where f is the focal length of the lens. For the same spacecraft and displaced height adopted in the InSAR mission, the focal length of 5 km will cost the extrapropellant mass of 0.05 kg/orbit (or day). Similarly, this Fresnel zone lens mission can merely achieve the continuous imaging around 0.2 deg latitude of the Earth. Assuming that the angle

between the thrust direction and lens, denoted by ξ, is still constant, to observe other latitudes δ, the orbit of the chief and follower should also be changed correspondingly according to the methodology above.

The sketch of the orientation baseline provided by the follower and the chief is shown in Fig. 14(a). To meet the condition of Earth surface–chief–follower on the same line, the off-axis equilibrium can be designed as $\Delta \mathbf{r}* = f \cdot [\cos(\eta - \delta), 0, \sin(\eta - \delta)]^T$, where δ is the latitude and η is changeable. For a specific value of η, there is only one displaced orbit of the chief that meets the requirement of the constant angle between the thrust direction and lens, and then the relative motion can be determined with $\Delta \mathbf{r}*$. Specially, when $\eta = \delta$, that is the case of the off-axis equilibrium lying along the x_o axis in the last simulation, the relationships between the observation latitude δ and the location of the chief's displaced orbit are the same with Fig. 13(b). As for other cases of $\eta \neq \delta$, the relationships between chief's displaced orbits and different angles η are shown in Fig. 14(b). It is indicated that the displaced height increases with the increasing angle η while the orbital radius decreases with the increasing angle η as well as the increasing latitude δ. Similarly to the advantages of displaced formation applied in InSAR measurements, the relative baseline vector for Earth imaging is fixed for the entire orbital period, which can realize the continuous imaging in any position of the displaced orbits.

5.2 Repeating Relative Ground Tracks for Phased Array Antenna Mission

In antenna theory, a phased array usually means an electronically scanned array that creates a beam of radio waves and electronically steers waves to point in different directions, without moving the antennas.[29] For the space-based phased array antenna mission, two basic requirements exist for the configuration geometry of the array antennas. The first requirement is to provide the repeating petal-like ground tracks on the y_o-z_o plane to revisit the surveillance area, and the second requirement is to assign numerous array antennas in a neat and regular manner. According to Sec. 3.2, the formation in resonant displaced heights will produce periodic relative trajectories rather than quasiperiodic trajectories, such as the 2:3 resonance resulting in polygonal-like relative ground tracks. Based on Sec. 3.3, the existence of off-axis equilibria by extracontrol of the follower will enable the assignment of array antennas in any position. Compared with the existing phased array antenna systems whose area is confined to a single satellite platform, phased array antenna missions in this paper are implemented with numerous satellites in displaced formation, which can largely expand the areas of array antenna and be used to monitor hot regions of the Earth.

In this mission, the phased array antenna system still has the same angular velocity and radius as the GEO, and the resonant height $h = 5570$ km is applied to generate resonant relative trajectory with $\omega_2 : \omega_3 = 2:3$. The array can be designed to various shapes such as the rectangle or circle for the specific requirements. Below are some examples to show applications of the off-axis equilibria in a phased array antenna system from the perspective of concept design.

For the rectangular array system, a 13×21 ($k = 7$, $l = 11$) array is assigned with the off-axis equilibria set to $\Delta r^* = [0 \quad (i - k)f(\Delta \bar{y}) \quad (j - l)g(\Delta \bar{z})]$, where $i = 1, \ldots, 13$, $j = 1, \ldots, 21$, the steps and $\Delta \bar{z}$ are the length of the
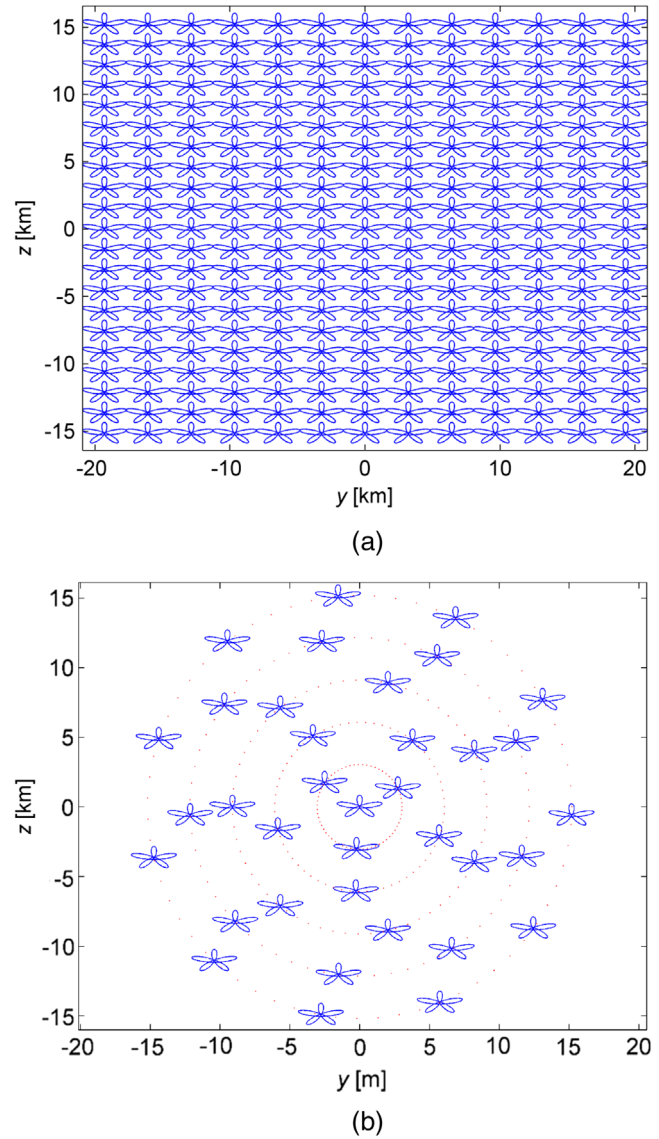

(a)

(b)

Fig. 15 Repeating relative ground tracks for a phased array antenna mission: (a) rectangular phased array antenna system and (b) circular phased array antenna system.

polygonal-like ground tracks in the row and column, respectively, and f and g are the functions of $\Delta \bar{y}$ and $\Delta \bar{z}$, respectively, which can be constant or in a regular change. With different rules of f and g, the phased array antenna system presents different configurations. Taking $f = (1 + (i - k)/2)\Delta \bar{y}$, $g = (1 + (j - l)/2)\Delta \bar{z}$ as an example, the antennas in rectangular array are denser in the middle than on the sides. In this case, the dense middle antennas can be used to monitor the target intensively and clearly, whereas the sparse side antennas monitor it globally and roughly. Particularly, for $f = \Delta \bar{y}$, $g = \Delta \bar{z}$ where $\Delta \bar{y} = 3.22$ m, $\Delta \bar{z} = 1.52$ m, the 13×21 ($k = 6$, $l = 10$) array is assigned with the antennas evenly distributed, as shown in Fig. 15(a). The extracontrol of the phased array antenna system in the **O** frame is $\mathbf{u}_o = \mathbf{B}\Delta \mathbf{r}*$, where **B** is the same form as Eq. (17). For the same spacecraft adopted above, the maximum extra-propellant mass per day for the phased array antenna is 0.00029 kg. The array can also be designed to concentric circles. For instance, the off-axis

equilibria are set to $\Delta r^* = \{\, 0 \quad 2\Delta\bar{z}(m-1)\cos\left[\frac{2\pi(n-1)}{2m-1} + \frac{\pi}{7}(m-1)\right] 2\Delta\bar{z}(m-1)\sin\left[\frac{2\pi(n-1)}{2m-1} + \frac{\pi}{7}(m-1)\right]\,\}$, where $m = 1,\ldots,6, n = 1,\ldots,2m-1$. The number of antennas in this case increases gradually from the center to the brim, and the phased array antenna system is shown as Fig. 15(b). These examples are simulated to show the diversity of antenna arrangements. The off-axis equilibria can also be set to other rules for some specific requirements.

6 Conclusion

Formation flying in a displaced circular orbit by low thrust has potential applications in providing additional views in the northern hemisphere or southern hemisphere, compared with those provided by a classic Keplerian orbit. The linearized relative equations were described by both the spatial dynamics in Newtonian form and the reduced dynamics in Hamiltonian form. Via the method of eigenvalue decomposition, the natural frequencies are characterized by the displaced height, and separate from each other at a critical height that differentiates the structural stability, bifurcation, and instability. The fundamental motions achieved by the Jordan decomposition included the stationary multiequilibria, periodic, and quasiperiodic oscillations and maximum leaving or approaching velocity. The off-axis equilibrium case was analyzed by a proposed open-loop control, and the motions near it were proved to be the same as the previous numerical motions. The closed analytical forms of linearized relative motions were derived for all stable, bifurcating, unstable displaced height cases. The "zero" conditions of initial value to generate the naturally bounded relative trajectories were derived analytically, and the unbounded relative trajectories were operated to achieve boundedness by the two extraclosed-loop controls regardless of the initial values.

The solutions and controls of the linearized relative motions developed in this paper have potential applications in Earth surface imaging and cooperative communication. A fixed relative baseline vector is provided for the InSAR or Fresnel zone lens missions, and different orbits of formation are solved with a constant installation angle to achieve the observation of different altitudes of the Earth. Resonant relative trajectories and off-axis equilibria are applied to the repeating relative ground tracks for a phased array antenna mission, where various arrangements of antennas are designed for different requirements. The important contributions of this paper are as follows: first, both the foundational motions in the spatial dynamical model and closed analytical forms in the reduced dynamical model were achieved to describe linearized relative motions for all stable, bifurcating, and unstable cases; second, control strategies were developed to guarantee the boundedness of relative trajectories for arbitrary initial values. Third, applications of the displaced formations, which can provide a fixed relative baseline vector, remove the restrictions of interferometry or imaging in the position and time compared with the classical formations.

However, there still remain some open problems. For instance, the applications of displaced formation flying were investigated and discussed for the feasibility from the perspective of the trajectory design and did not involve in the performance evaluation of the instrument and equipment. This may be very hard and complicated work, which will be researched further in the next paper.

References

1. H. Dankowicz, "Some special orbits in the two-body problem with radiation pressure," *Celestial Mech. Dyn. Astron.* **58**(4), 353–370 (1994).
2. C. R. McInnes, "The existence and stability of families of displaced two-body orbits," *Celestial Mech. Dyn. Astron.* **67**(2), 167–180 (1997).
3. C. R. McInnes, "Dynamics, stability, and control of displaced non-Keplerian orbits," *J. Guid. Control Dyn.* **21**(5), 799–805 (1998).
4. M. Xu and S. J. Xu, "Nonlinear dynamical analysis for displaced orbits above a planet," *Celestial Mech. Dyn. Astron.* **102**(4), 327–353 (2008).
5. S. B. Broschart and D. J. Scheeres, "Control of hovering spacecraft near small bodies: application to asteroid 25143 Itokawa," *J. Guid. Control Dyn.* **28**(2), 343–354 (2015).
6. L. Niccolai, A. A. Quarta, and G. Mengali, "Electric sail elliptic displaced orbits with advanced thrust model," *Acta Astronaut.* **138**, 503–511 (2017).
7. C. R. McInnes, "Displaced non-Keplerian orbits using impulsive thrust," *Celestial Mech. Dyn. Astron.* **110**(3), 199–215 (2011).
8. J. Heiligers et al., "Displaced geostationary orbit design using hybrid sail propulsion," *J. Guid. Control Dyn.* **34**(6), 1852–1866 (2011).
9. R. McKay et al., "Survey of highly non-Keplerian orbits with low-thrust propulsion," *J. Guid. Control Dyn.* **34**(3), 645–666 (2011).
10. M. Macdonald et al., "Low-thrust-enabled highly-non-Keplerian orbits in support of future mars exploration," *J. Guid. Control Dyn.* **34**(5), 1396–1411 (2011).
11. K. Alfriend et al., *Spacecraft Formation Flying: Dynamics, Control and Navigation*, Butterworth-Heinemann, Oxford (2009).
12. J. D. Biggs and C. R. McInnes, "Solar sail formation flying for deep-space remote sensing," *J. Spacecr. Rockets* **46**(3), 670–678 (2009).
13. S. P. Gong, H. X. Baoyin, and J. P. Li, "Solar sail formation flying around displaced solar orbits," *J. Guid. Control Dyn.* **30**(4), 1148–1152 (2007).
14. S. P. Gong, J. P. Li, and H. X. Baoyin, "Formation around planetary displaced orbit," *Appl. Math. Mech.* **28**(6), 759–767 (2007).
15. W. Wang et al., "Invariant manifold and bounds of relative motion between heliocentric displaced orbits," *J. Guid. Control Dyn.* **39**(8), 1764–1776 (2016).
16. W. Wang et al., "Extreme values of relative distances for spacecraft in elliptic displaced orbits," *Adv. Space Res.* **58**(4), 475–487 (2016).
17. W. Wang et al., "Analysis of relative motion in non-Keplerian orbits via modified equinoctial elements," *Aerosp. Sci. Technol.* **58**, 389–400 (2016).
18. J. Bookless and C. R. McInnes, "Dynamics and control of displaced periodic orbits using solar-sail propulsion," *J. Guid. Control Dyn.* **29**(3), 527–537 (2006).
19. Y. She and S. Li, "Optimal slew path planning for the Sino-French space-based multiband astronomical variable objects monitor mission," *J. Astron. Telesc. Instrum. Syst.* **4**(1), 017001 (2018).
20. Z. H. Dang and H. Zhang, "Linearized relative motion equations through orbital element differences for general Keplerian orbits," *Astrodynamics* **2**(3), 201–215 (2018).
21. D. J. Scheeres, F. Y. Hsiao, and N. X. Vinh, "Stablizing motion relation to an unstable orbit: applications to spacecraft formation flight," *J. Guid. Control Dyn.* **26**(1), 62–73 (2003).
22. M. Xu and S. J. Xu, "Structure-preserving stabilization for Hamiltonian system and its applications in solar sail," *J. Guid. Control Dyn.* **32**(3), 997–1004 (2009).
23. S. Soldini, C. Colombo, and S. Walker, "Comparison of Hamiltonian structure-preserving and Floquét mode station-keeping for libration-point orbits," in *AIAA/AAS Astrodynamics Specialist Conf.*, AIAA SPACE Forum, AIAA 2014–4118 (2014).
24. J. Zhang and Z. Zhang, "Deployment research of multi-tethered InSAR system for GMTI mission," in *Geoscience and Remote Sensing Symp.*, IEEE, pp. 4792–4795 (2016).

25. M. Xu, Y. H. Jia, and S. J. Xu, "The J_2 invariant relative configuration of spaceborne SAR interferometer for digital elevation measurement," *Acta Mech. Sin.* **26**(4), 643–651 (2010).
26. G. Krieger et al., "Interferometric synthetic aperture radar (SAR) missions employing formation flying," *Proc. IEEE* **98**(5), 816–843 (2010).
27. G. Krieger et al., "TanDEM-X: a satellite formation for high-resolution SAR interferometry," *IEEE Trans. Geosci. Remote Sens.* **45**(11), 3317–3341 (2007).
28. A. K. Srivastava et al., "Micro-patterned photo-aligned ferroelectric liquid crystal Fresnel zone lens," *Opt. Lett.* **40**(8), 1643–1646 (2015).
29. R. E. Wallis and S. Cheng, "Phased-array antenna system for the MESSENGER deep space mission," in *IEEE Aerospace Conf. Proc. (Cat. No. 01TH8542)*, pp. 41–49 (2001).

Xiao Pan received her BS degree from the School of Astronautics from Northwestern Polytechnical University, Shaanxi, China, in 2015. She is currently completing her PhD in spacecraft design and engineering at Beijing University of Aeronautics and Astronautics, Beijing, China. Her research interests include the circular restricted three-body problem, trajectory design, navigation technology, and formation flying.

Ming Xu received his BS and PhD degrees in aerospace engineering from Beihang University, Beijing, China, in 2003 and 2008, respectively. He served as an engineer of orbital design and operation in DFH Satellite Co., Ltd., China Academy of Space Technology, Beijing, China, until 2010. Then, he joined in Beihang University as an assistant professor, and was promoted as an associate professor in 2012. His current research interests include the applications of dynamical systems theory into astrodynamics and orbital control. He serves as associate editor for the journals of *Astrodynamics*, and *Advances in Aircraft and Spacecraft Science*. He received National Top 100 Excellent Doctoral Dissertations Award nomination in 2010 and third class prizes of the National Defense Technology Invention Award in 2016. He has 50 publications in journals, books and proceedings.